Analysis and Augmented Model-Based Control Design of Distributed Generation Converters With a Flexible Grid-Support Controller

Shahed Mortazavian, *Student Member, IEEE*, and Yasser Abdel-Rady I. Mohamed, *Senior Member, IEEE*

***Abstract*—Supporting the host grid during voltage dips has become a major connection requirement for large distributed generation units. Because most of the grid faults are unsymmetrical, the recently developed grid codes suggest the injection of a flexible positive- and negative-sequence reactive current components proportional to the magnitude of the voltage dip at the point of common coupling. However, detailed dynamic analysis of the augmented grid-connected converter with the flexible positive- and negative-sequence current injection function and the characterization of the impact of the grid strength, converter control parameters, and proportionality constants used in the reference current generation block are not reported in the literature. To fill in this gap, first, a multi-stage linear model of the augmented nonlinear system dynamics is developed, and the small-signal stability analysis is performed on the system dynamic behavior before, during, and after the fault. The effects of different system and control parameters are studied and characterized. Second, a new and effective model-based controller design method is proposed to maintain the system stability during and after the fault with the consideration of the mutual interaction among different system controllers. Finally, the time-domain simulations and laboratory experiments validate the accuracy and effectiveness of the proposed control method.**

***Index Terms*—Distributed generation (DG), modeling, multi-sequence, reactive current injection, small-signal stability analysis, symmetrical components, unbalanced fault, unbalanced grid.**

NOMENCLATURE

A. Superscripts

$+$	Positive-sequence components.
-	Negative-sequence components.
$*$	Variable reference value.
ss	Steady-state value.

B. Subscripts

d	Variable component in the d-axis.
q	Variable component in the q-axis.

C. Variables and Parameters

i_g	Grid current.

Manuscript received March 11, 2018; revised June 28, 2018 and September 3, 2018; accepted October 3, 2018. Date of publication October 17, 2018; date of current version May 2, 2019. This work was supported by the Natural Sciences and Engineering Research Council of Canada (NSERC). Recommended for publication by Associate Editor L. Peng. *(Corresponding author: Shahed Mortazavian.)*

The authors are with the Department of Electrical and Computer Engineering, University of Alberta, Edmonton, AB T6G 2R3, Canada (e-mail:

DG units to remain connected and improve the voltage profile during short-term grid faults. Accordingly, the capability of low-voltage ride-through (LVRT) is nowadays an important mandate for the converter-interfaced DG (CI-DG) units [4]–[7]. In the German standards, i.e., E.ON and VDN [8], [9], and the recent European code, i.e., ENTSO-E [10], large wind power plants are expected to stay connected even when there is a voltage sag down to zero. To maintain the stability of the power system, DG units are also expected to inject reactive current proportional to the voltage drop, with a deadband applied to the voltage deviation [11].

To comply with the new grid code requirements, the CI-DG units are designed such that the active and reactive current injection to the grid is controlled independently by a grid-connected converter (GCC) considering the maximum current capacity of the converter [11]–[14]. As a conventional approach, the reactive current is injected as per grid code requirement, and any remaining capacity is utilized for the active power injection. However, in [11], it was shown that wind power plants might lose their synchronism with the grid fundamental frequency during severe faults. This, not only, does not support the voltage during the LVRT, but even worsens the situation. A phase-locked loop (PLL) frequency-based active current injection algorithm is then introduced in [11] to solve the loss of a synchronism problem. The impact of the bandwidth of the dc and ac voltage controllers on the system stability during a grid fault was studied through the small-signal analysis in [15]. In this study, time-domain simulations are carried out to guarantee the stability of the system in the case of large disturbances. However, neither [11] nor [15] studied the effect of any unbalanced grid fault on the LVRT performance of the GCCs.

The injected currents into the grid may include negative-sequence components to impede the effects of the unbalanced fault. The most common way to control a current vector with positive- and negative-sequence components is to design the current controller based on two synchronous reference frames [13]–[20], [22], with the value of their rotating frequency equal to the fundamental grid frequency, but in the positive and negative directions.

In addition to the nonlinear dynamics of a GCC (e.g., due to the PLL), the presence of the reactive reference current generation (RCG) proportional to the voltage dip magnitude adds more coupling between the converter-injected current and the grid voltage at the point of common coupling (PCC). However, the existing literature lacks the study of the modeling and dynamic analysis of the DG units equipped with the RCG controllers based on the new LVRT standards [9], [21]. The new LVRT standards [9], [21] require the DG units to not only stay connected to the grid, but also inject both positive- and negative-sequence reactive currents proportional to the unbalanced voltage sag characteristics under severe short-term unbalanced grid faults. In the following, this important requirement will be referred to as required positive- and negative-sequence injection and low-voltage ride-through (RPNSI-LVRT) requirement. The existing study in the literature on the dynamic behavior of the converters under unbalanced conditions [13], [20] only deals with the four conventional RCG techniques, none of which requires a certain amount of reactive current injection under the unbalanced faults. These conventional RCGs are only responsible for having the basic LVRT capability (and not the RPNSI-LVRT capability), which means the GCC is only required to stay connected under unbalanced conditions. In this sense, the RPNSI-LVRT capability has an additional requirement of injecting both positive- and negative-sequence reactive currents proportional to the unbalanced voltage sag characteristics. Therefore, in addition to the nonlinear dynamics of a GCC, the presence of the RPNSI-LVRT adds more coupling and complexity to the system in dynamic, transient, and stability studies. The presence of the RPNSI-LVRT requirement may lead to critical instability problems under different conditions, e.g., severe unbalanced faults, weak grid conditions, and conventionally tuned control parameters. This is a significant difference between the conventional LVRT requirements [7], [8] and the newly imposed RPNSI-LVRT requirement [9], [21] under short-term unbalanced faults. In Section II, the flexible multi-sequence reactive current injection (FMS-RCI) technique [21] is presented to meet the RPNSI-LVRT requirement, which uses two control parameters (i.e., K^+ and K^-) to inject the positive- and negative-sequence reactive currents, respectively, proportional to the amount of the positive-sequence voltage drop and negative-sequence voltage rise.

To fill in the existing gaps in the literature and solve the aforementioned problems, the following contributions are accomplished in this paper. In Section III, a multi-stage linearized state-space model (i.e., before, during, and after the fault models) is developed for a DG unit to analyze the dynamic performance and stability of the system under the RPNSI-LVRT requirement. This method provides the possibility of studying the imposed RCG methods before and during the unbalanced faults with different operating points. The impact of two coefficients, K^+ and K^-, in the FMS-RCI technique on the dynamic performance and the transient stability of the DG control system is studied in Section IV. A model-based control parameter design is then proposed, in Section V, to find suitable values for K^+ and K^- parameters in weak grid conditions for stability purposes under RPNSI-LVRT requirements. The interactions between different converter controllers (e.g., current control and PLL) and the FMS-RCI controller, in the decoupled double synchronous reference frame (DDSRF), are studied, and their impact on the system stability is analyzed using the small-signal stability analysis. The parameters of the current controller are also designed based on the developed state-space model to have the RPNSI-LVRT capability. In Section VI, the developed models and the proposed techniques are also applied to a more complex system with two DG units to consider the interactions between DG units on the RPNSI-LVRT performance of the entire system, while using the FMS-RCI method. Finally, the proposed analytical design methods are tested using experimental test cases in Section VII. The results are promising and demonstrate the effectiveness of the developed models and proposed approaches in improving the stability of the DG systems under severe unbalanced faults when the RPNSI-LVRT is required by the grid code. Section VIII concludes this work.

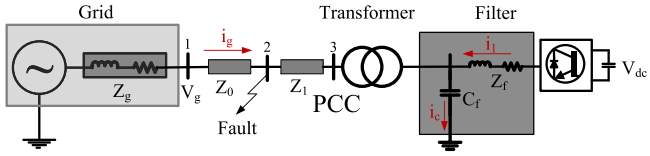

Fig. 1. CI-DG unit.

TABLE I
SYSTEM PARAMETERS

DG unit		Line Parameters (p.u.)		System Parameters
Rating	5.0 MVA, 480 V			System rated voltage: 27.6 kV
V_{dc}	1.2 kV	Z_0	0.0068 + 0.0845i	System rated power:
C_{dc}	12 mF	Z_1	0.0017 + 0.0042i	10 MVA (base power)
R_f, L_f	2 mΩ, 100 μH			Short-Circuit Ratio (SCR): 5.5

II. CI-DG UNIT AND THE LVRT REQUIREMENTS

Fig. 1 represents a CI-DG unit, which is designed based on a typical Northern Ontario, Canada, rural distribution system. It consists of a 27.6-kV radial distribution system connected to a dispatchable three-wire DG unit. The DG unit is connected to the medium-voltage feeder via a step-up Y/Δ transformer. PCC on bus3 stands for the point of common coupling. The system parameters are given in Table I.

The grid frequency synchronization and active/reactive current control procedure are performed at the low-voltage side of the GCC. The DG current controller is designed in the DDSRF on the *dq* coordinates, with the rotating frequencies in the positive and negative directions with respect to the fundamental grid frequency; hence, it controls the positive- and negative-sequence current components.

During normal operation, the implemented current controller in the DDSRF receives its reference values based on the active and reactive power demands by the upstream system or the DG unit. Therefore, the reference currents are generated according to the following equations:

$$i_{1d}^{*+} = \frac{2}{3}\frac{P^*}{V^+_{pd}}, \quad i_{1d}^{*-} = 0 \tag{1}$$

$$i_{1q}^{*+} = \frac{-2}{3}\frac{Q^*}{V^+_{pd}}, \quad i_{1q}^{*-} = 0. \tag{2}$$

Based on the conventional LVRT standards on the voltage limits [7], [8], the CI-DG system is supposed to follow the grid code requirements, presented in Fig. 2, and remains connected to the grid when a fault occurs. The typical reactive current injection curve of this grid code is shown in Fig. 2(b), which implies that in the case of a voltage sag less than 50%, the per unit (p.u.) reactive current injection is proportional to the p.u. value of the voltage sag with the slope of 2. Besides, based on this grid code, when the voltage sag is more than 50%, the whole thermal limit is devoted to the reactive current injection (i.e., $i_q = 1$ p.u.). Besides, according to this grid code for Type 2 generating plants, which include the system under study in

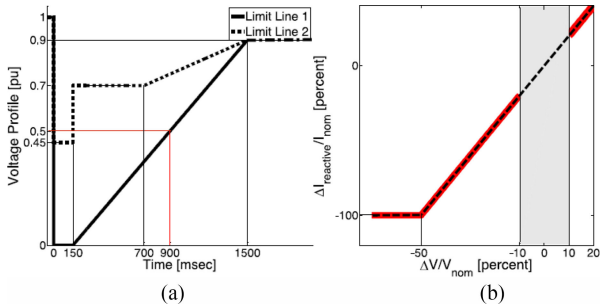

Fig. 2. German E.ON. Grid code for LVRT [8]. (a) Voltage limits. (b) Reactive current injection.

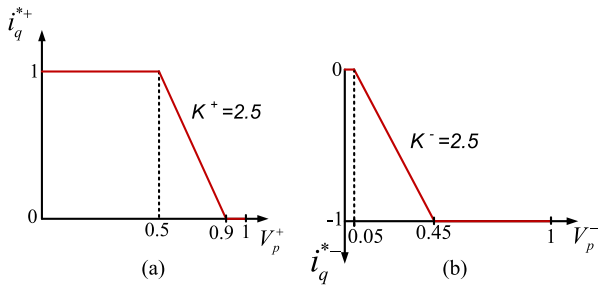

Fig. 3. Reactive current injection based on the new grid codes [9]. (a) FPS-RCI. (b) FNS-RCIs.

this paper, it is required that "three-phase short circuits or fault-related symmetrical voltage dips must not lead to instability above the Limit Line 1 in Fig. 2 or to disconnection of the generating plant from the grid" [8]. However, this standard did not distinguish between the negative and positive components of the reactive current injection.

The injection of negative-sequence current has been recently presented in the German grid code, VDE-AR-N 4120 [9]. This code was published in 2015 describing the connection of generation plants to the high-voltage network and, for the first time, requiring the negative-sequence current injection by these units in the case of the unbalanced faults.

As mentioned earlier, this is referred to as the RPNSI-LVRT requirement in this paper. Under unbalanced grid faults, the classical synchronous generators provide short-circuit current, which consists of the positive- and negative-sequence currents. On the other hand, DG units or transmission systems such as high-voltage dc or flexible ac transmission systems with a fully rated voltage-source converter (VSC) usually repress the negative-sequence current [23]. Generally, the converter of these units employs a decoupled current controller on positive and negative sequences. Therefore, the current objective is to independently control both sequence components to meet the requirements of the new grid codes. In this paper, two different equations are used for the injection of the symmetrical components of the reactive current in each sequence. From now on, this method is called the FMS-RCI, which is obtained based on the recent German grid code [21]. As illustrated in Fig. 3(a), the condition for the flexible positive-sequence reactive current injection (FPS-RCI) is almost the same as the one imposed in

Fig. 2(b), but the flexible slope of the ratio of the i_q^{*+} injection to the positive-sequence voltage dip is defined as K^+.

On the other hand, the flexible negative-sequence reactive current injection (FNS-RCI) is proportional to the negative-sequence voltage value when it is higher than 0.05% with the flexible slope of K^-. The whole criteria on both components for the case of $K^+ = K^- = 2.5$ can be expressed as follows:

$$\text{FPS} - \text{RCI}:$$

$$\begin{cases} eq_1^+: & \Delta V_p{}^+ > 90\% \;\rightarrow\; i_q^{*+} = \frac{-2}{3}\frac{Q^*}{V^+{}_{pd}} \\ eq_2^+: & 50\% < \Delta V_p{}^+ < 90\% \;\rightarrow\; i_q^{*+} = K^+ \Delta V_p{}^+ \\ & \qquad\qquad\qquad = K^+(0.9 - V_p{}^+)_{\text{p.u.}} \\ eq_3^+: & \Delta V_p{}^+ < 50\% \;\rightarrow\; i_q^{*+} = 1\,\text{p.u.} \end{cases} \tag{3}$$

$$\text{FNS} - \text{RCI}:$$

$$\begin{cases} eq_1^-: & \Delta V_p{}^- < 5\% \;\rightarrow\; i_q^{*-} = 0 \\ eq_2^-: & 5\% < \Delta V_p{}^- < 45\% \;\rightarrow\; i_q^{*-} = K^- \Delta V_p{}^- \\ & \qquad\qquad\qquad = K^-(0.05 - V_p{}^-)_{\text{p.u.}} \\ eq_3^-: & \Delta V_p{}^- > 45\% \;\rightarrow\; i_q^{*-} = -1\,\text{p.u.} \end{cases} \tag{4}$$

For example, if the positive-sequence voltage drops below 50%, there will be 1.0 p.u. of the positive-sequence reactive current injection. If the total magnitude of the injected reactive current (obtained from the positive and negative sequences) reaches the maximum thermal limit of the converter, the active current injection will be set to zero. Otherwise, while the peak value of the total injected current (active and reactive) does not exceed the thermal limit, the value of the active current will be obtained from (1). The schematic diagram of the FMS-RCI method is shown in Fig. 4.

Any oscillation on the positive sequence of the PCC voltage (V_{pd}^+) appears in $\frac{\partial i_d^{*+}}{\partial V_{pd}^+}$, which is directly presented in the linearization of (1). Therefore, the RCG block is affected by the variations of the PCC voltage. This will take the system modes to the unstable region, which may result in the operation of the protection devices and LVRT failure. Therefore, to improve the stability performance of the system, a low-pass filter (LPF) with the time constant of 3 ms is employed on the positive sequence of the PCC voltage in the RCG block, as shown in Fig. 4. To illustrate the effectiveness of using this filter, the time-domain simulation results are presented in Fig. 5. In this test case, the RCG method is switched to the FMS-RCI at $t = 0.3$ s. As shown in Fig. 5(a), the generated reference current in the *dq* frame gets unstable after 50 ms when there is no LPF applied on the positive-sequence voltage extraction on the PCC. However, when the LPF is applied, the generated current is remained stable and steady. This effect is also visible in Fig. 5(b), where the three-phase signal of the PCC voltage is demonstrated at the same test case. The importance and the effectiveness of the application of this LPF are also studied using the eigenvalue analysis, and the results are presented in Section IV-B.

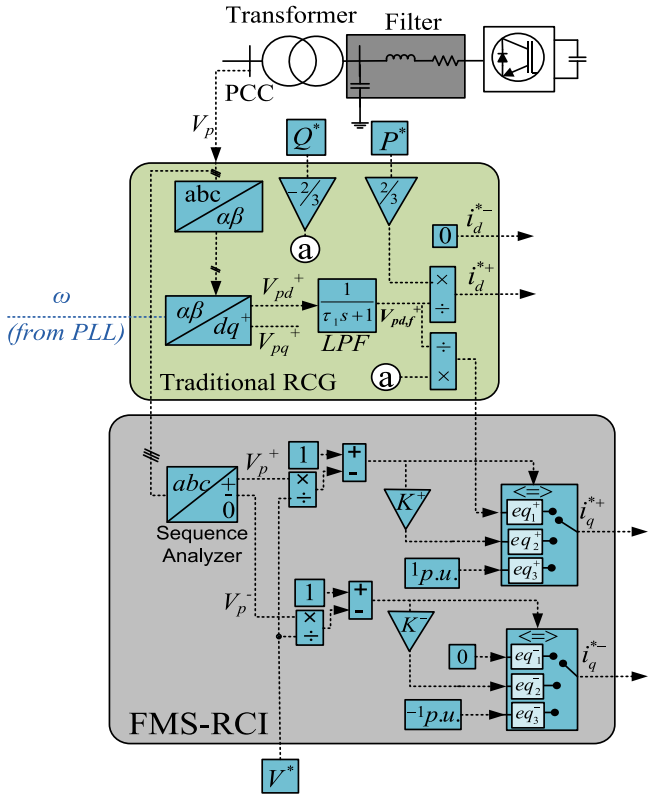

Fig. 4. RCG diagram.

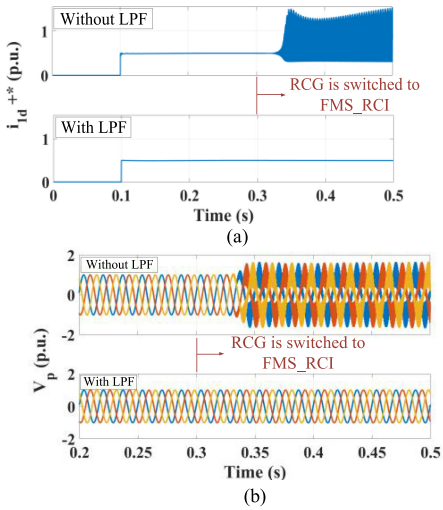

Fig. 5. Effect of using the low-pass filter in the implementation of the RCG block on (a) the generated reference current in the d^+ frame, and (b) the three phase signal of the PCC voltage.

III. Multi-Stage Linearized Model

The dynamics of the GCC are highly nonlinear. Besides, according to (1)–(4) and because there are many feedback loops through LPFs (in the implementation of the current controller and the PLL), they add more non-linearity to the system. To obtain a detailed small-signal stability analysis in this paper, the complete CI-DG unit system in the DDSRF is linearized

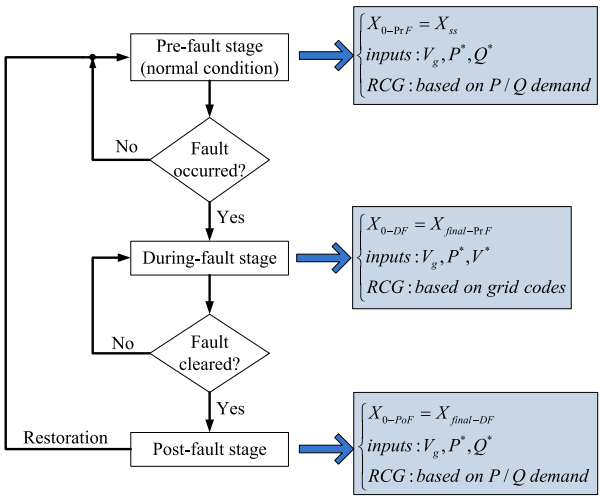

Fig. 6. Diagram of the multi-stage modeling.

in three different stages: before, during, and after the fault. This multi-stage state-space modeling is obtained based on the approach presented in [24].

During a fault, the converter loses its capability, partially or completely, to inject or absorb active power, so a voltage violation may occur. To prevent any disconnection of the DG unit during the fault, switching the RCG method from (2) to (3) and (4) is proposed based on the grid codes. In this paper, the performance of an LVRT-capable CI-DG unit system is analyzed analytically.

Obtaining the linearized models for a CI-DG unit is essential to analyze its dynamic performance during LVRT and to set up different controllers. A CI-DG unit will be subjected to different operating conditions under the fault; hence, employing one linearized model does not seem reasonable. Therefore, three stages are adopted in this paper for accurate modeling, while considering the LVRT requirements. The first stage represents the CI-DG unit system dynamics before the fault occurrence. In this stage, the model input consists of the measured grid bus voltage (V_g) and the value of the active and reactive power demands (P^* and Q^*, respectively). Also, the employed RCG method is based on (1) and (2). The steady-state values for the first stage are obtained from the normal system operation.

The second stage characterizes the CI-DG unit system dynamics during the fault period, where the generated reference currents are dictated by new LVRT requirements, presented in (3) and (4). The model inputs in this stage are V_g, the active power demand, and the reference PCC voltage value (V^*).

The third stage represents the CI-DG unit system dynamics after fault clearance. Current system dynamics, which is changed from its steady-state mode during the fault, tries to recapture the pre-fault condition. In this stage, the system is mainly reacting to its initial states instead of any external forces. This initial state is the final state obtained from the second stage, i.e., during-fault stage. The schematic diagram is illustrated in Fig. 6. Subscripts *0* and *final* stand for the initial and final states, respectively, SS stands for the steady state, and, PrF, DF, and PoF stand for the pre-fault, during-fault, and post-fault stages, respectively. Each stage and the related linearized models will be discussed in the following subsections.

In all stages, the generated reference current signals are fed into four proportional–integral (PI) regulators implemented in the DDSRF. This controlling section is the same in all modeling stages; however, the method of generating the reference current values, the initial states, and the input matrices is different. Because the RCG is an outer loop compared to the current controller, it should have a slower response time. Therefore, an LPF with the time constant of τ_1 is designed on V_{pd}^+ sampling to implement (1) and (2). The relation between the actual and the reference currents in *dq* frames, for both sequences, can be approximated by

$$i_{d(q)} = \frac{1}{\tau_i s + 1} i_{d(q)}^* \tag{5}$$

where τ_i is the time constant of the closed-loop current controller [25]. Therefore, the value of τ_1 should be chosen carefully compared to τ_i. The effect of using the LPF on the system stability will thoroughly be discussed in Section IV.

To obtain a detailed linearized model for the system with the consideration of all controllers, 23 state variables are defined as follows:

$$\begin{aligned} X_{23\times 1} = \Big[& i_{gd}^+, i_{gq}^+, i_{gd}^-, i_{gq}^-, i_{1d}^+, i_{1q}^+, i_{1d}^-, i_{1q}^-, \\ & \int e_d^+ dt, \int e_q^+ dt, \int e_d^- dt, \int e_q^- dt, \omega, v_{pd}^+, v_{pq}^+, \\ & v_{pd}^-, v_{pq}^-, v_{fd}^+, v_{fq}^+, v_{fd}^-, v_{fq}^-, v_{pd,f}^+, v_{pq,f}^+ \Big]^T \end{aligned} \tag{6}$$

where $\int e\, dt$ stands for the integral of the current signal error and $V_{p,f}^+$ stands for the output signal of the LPF, which is used on sampling the V_{pd}^+ (see Fig. 4).

The standard linearized form of the state-space equations as $\Delta \dot{X} = A\,\Delta X + B\,\Delta U$ and $\Delta Y = C\,\Delta X + D\,\Delta U$ are used in obtaining the multi-stage system model. According to the number of state variables, there will be 23 differential equations when obtaining the state-space model of the system. Therefore, to simplify the representation of the overall model, the following mathematical method is used in this paper to obtain the final state and input matrices:

$$\begin{aligned} & \Delta \dot{X} = A_2\,\Delta \dot{X} + A_1\,\Delta X + B_1\,\Delta U \Rightarrow \\ & (I - A_2)\Delta \dot{X} = A_1\,\Delta X + B_1\,\Delta U \Rightarrow \\ & \Delta \dot{X} = \underbrace{(I - A_2)^{-1} A_1}_{A}\,\Delta X + \underbrace{(I - A_2)^{-1} B_1}_{B}\,\Delta U. \end{aligned} \tag{7}$$

Therefore, the final state and input matrices would be $A = (I - A_2)^{-1} A_1$ and $B = (I - A_2)^{-1} B_1$, respectively.

A. Pre-Fault Stage

The first stage characterizes the CI-DG unit dynamics before the fault occurrence. In this stage, the reference current signals are generated based on (1) and (2) to be fed into the four PI regulators implemented in the negative and positive sequences

in the *dq* reference frames. In this stage, the model inputs include the active and reactive power demands required by the system operators (i.e., P^* and Q^*). The input matrix for the pre-fault stage is

$$u = \left[v_{gd}^+, v_{gq}^+, v_{gd}^-, v_{gq}^-, P^*, Q^*\right]. \tag{8}$$

In the pre-fault stage modeling, the origin is considered as the equilibrium point, which is obtained in the normal operating condition of the CI-DG unit system. The final linearized forms of (1) and (2) can be easily obtained as follows:

$$\begin{aligned}
\Delta i_d^{*+} &= \frac{2}{3}\frac{1}{V^+{}_{pd,f,ss}}\Delta P^* + \frac{2}{3}{P_{ss}}^*\frac{-1}{\left(V^+{}_{pd,f,ss}\right)^2}\Delta V^+{}_{pd,f} \\
\Delta i_q^{*+} &= \frac{-2}{3}\frac{1}{V^+{}_{pd,f,ss}}\Delta Q^* + \frac{-2}{3}{Q_0}^*\frac{-1}{\left(V^+{}_{pd,f,ss}\right)^2}\Delta V^+{}_{pd,f} \\
\Delta i_d^{*-} &= 0, \Delta i_q^{*-} = 0
\end{aligned} \tag{9}$$

where the subscript *ss* stands for the steady-state values. The detailed linearized equations for the PLL and the current controller can be found in [20]. Using (6)–(9), the state-space matrices can be defined as presented in the Appendix.

B. During-Fault Stage

The second stage considers the CI-DG unit dynamics during the fault period, where the RCG is dictated by the LVRT requirements. In this paper, the FMS-RCI method will be used to meet the new grid codes requirements. The related equations are shown in (3) and (4). It can be seen that in each sequence of the reactive current reference generation, three different equilibrium points are considered based on the positive-sequence voltage drop (in FPS-RCI) and the value of the negative-sequence voltage (in FNS-RCI). These equilibrium points are shown in (3) and (4) by eq_i^+ and eq_i^-, in which *i* can be 1, 2, or 3.

In this case, the model input contains P^* and V_p^*. The input matrix for the during-fault stage is

$$u = \left[v_{gd}^+, v_{gq}^+, v_{gd}^-, v_{gq}^-, P^*, V_p^*\right]. \tag{10}$$

For the studied fault in this paper, both PCC voltage sequences are in the intervals of eq_2^+ and eq_2^- of (3) and (4) during the fault (i.e., $50\% < \Delta {V_p}^+ < 90\%$ and $5\% < \Delta {V_p}^- < 45\%$), and the total value of the injected reactive current is below 1.0 p.u. Since the total injected current also remained below the thermal limit, the injection of the active current is based on (1). Therefore, the linearized form of the injected active current would be the same as presented in (9) for Δi_d^{*+} and Δi_d^{*-}. The reference current values in the *q* frame are calculated based on (3) and (4) to implement the FMS-RCI method for LVRT performance. Therefore, the linearized equations for eq_2^+ and eq_2^-, which are the most complicated equilibrium points, are presented here

$$\begin{aligned}
\Delta i_q^{*+} &= K^+\left(\Delta V^* - \Delta\sqrt{{v_{pd}^+}^2 + {v_{pq}^+}^2}\right) \\
&= K^+(\Delta V^* - m_{11}\Delta v_{pd}^+ - m_{21}\Delta v_{pq}^+)
\end{aligned} \tag{11}$$

$$\begin{aligned}
\Delta i_q^{*-} &= -K^-\left(\Delta\sqrt{{v_{pd}^-}^2 + {v_{pq}^-}^2}\right) \\
&= K^-(-m_{31}\Delta v_{pd}^- - m_{41}\Delta v_{pq}^-)
\end{aligned} \tag{12}$$

in which

$$m_{11} = \frac{v_{pd,ss}^+}{\sqrt{{v_{pd,ss}^+}^2 + {v_{pq,ss}^+}^2}}, \quad m_{21} = \frac{v_{pq,ss}^+}{\sqrt{{v_{pd,ss}^+}^2 + {v_{pq,ss}^+}^2}} \tag{13}$$

$$m_{31} = \frac{v_{pd,ss}^-}{\sqrt{{v_{pd,ss}^+}^2 + {v_{pq,ss}^+}^2}}, \quad m_{41} = \frac{v_{pq,ss}^-}{\sqrt{{v_{pd,ss}^+}^2 + {v_{pq,ss}^+}^2}}. \tag{14}$$

Based on these equations, A_1, A_2, and B_1 matrices are obtained to provide the final complete linear model of the during-fault stage, using (7). For space saving, only those A_1 matrix elements of the during-fault model are shown in (15), which are different from the A_1 elements of the pre-fault stage [see (A1)–(A5)]:

$$\begin{aligned}
&A_1(10,14) = K^+(-m_{11}),\ A_1(10,15) = K^+(-m_{21}), \\
&\qquad A_1(10,22) = 0, \\
&A_1(12,16) = K^-(-m_{31}),\ A_1(12,17) = K^-(-m_{41}).
\end{aligned} \tag{15}$$

The A_2 matrix, for the during-fault stage, is the same as the pre-fault stage [i.e., with the nonzero elements presented in (A6)]. Finally, for B_1, the only different element between (A7) and the B_1 matrix of the during-fault stage model is

$$B_1(10,6) = K^+. \tag{16}$$

Using these equations, the complete linear model for the during-fault stage is also obtained. Model initialization is made using the steady-state values of system parameters during the fault. Based on the grid code standards of Fig. 2, system performance during the first 150 ms from the fault occurrence is the primary concern in the LVRT studies [8]. Therefore, the steady-state values for this stage are obtained from the final states of this 150-ms period.

C. Post-Fault Stage

This stage characterizes the CI-DG unit dynamics after the fault clearance when the system is trying to retrieve its normal condition, which is the initial pre-fault operating point. Therefore, (1) and (2) are again valid to represent the RCG method, and the same linear model as the pre-fault stage [i.e., (9) and (A1)–(A7)] can be used in this stage. However, the origin is not the equilibrium point anymore. Instead, the corresponding initial point can be easily extracted from the final states of the during-fault stage.

The main focus of this paper is on the during- and post-fault stages because these models make it possible to study the dynamics of the FMS-RCI method considering the LVRT requirements. In fact, the effect of the flexible selection of K^+, K^-, and other controlling parameters on system stability performance during and after a fault can be thoroughly studied in this model

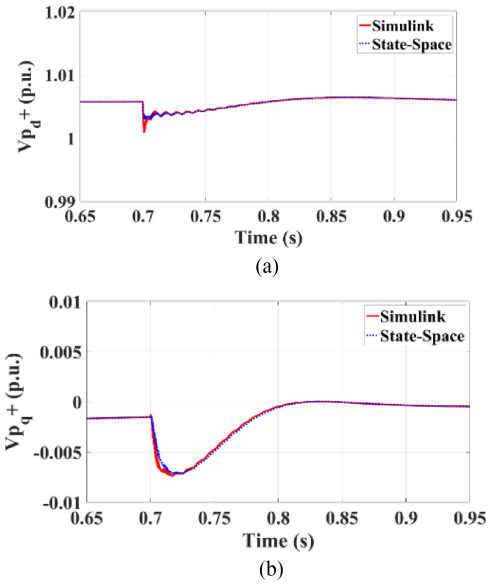

Fig. 7. State-space model validation for (a) the positive d-axis and (b) the positive q-axis PCC voltage when the reference active power drops by 10%.

with the consideration of different grid strengths and unbalanced fault characteristics.

D. Model Verification

To verify the effectiveness of the obtained linear model, the time-domain response of the state-space model is compared to the time-domain response of the detailed nonlinear model simulated in MATLAB-SIMULINK. The model validation results show an accurate agreement between both models responses. A sample case is shown in Fig. 7. In this case, the system is operating in the pre-fault situation, and the DG active power reference drops by 10% at $t = 0.7$ s. Fig. 7 shows a comparison of the positive d- and q-axis PCC voltage in the linear and nonlinear models. Both figures show the accuracy of the obtained state-space model as the two traces are nearly identical.

IV. Stability Analysis Considering RPNSI-LVRT Requirements

To implement the FMS-RCI, the diagrams of Figs. 3 and 4 are used in this paper. The initial design of the PI compensators in the current controller and the PLL is based on the gain-shaping method presented in [25]. Besides, Sharifabadi *et al.* [21] suggest selecting the typical value of 2.5 for both K^+ and K^-, while the system is in eq_2^+ and eq_2^-, respectively. This value determines the ratio of the reactive current injection in both positive and negative sequences with respect to the positive-sequence voltage dip and negative-sequence voltage value.

A. FMS-RCI Performance in LVRT

One of the missing studies in the literature is a thorough analysis of the effect of the grid strength on the stability performance of the CI-DG unit while employing the FMS-RCI. The nature of CI-DG system interactions with the power system and their

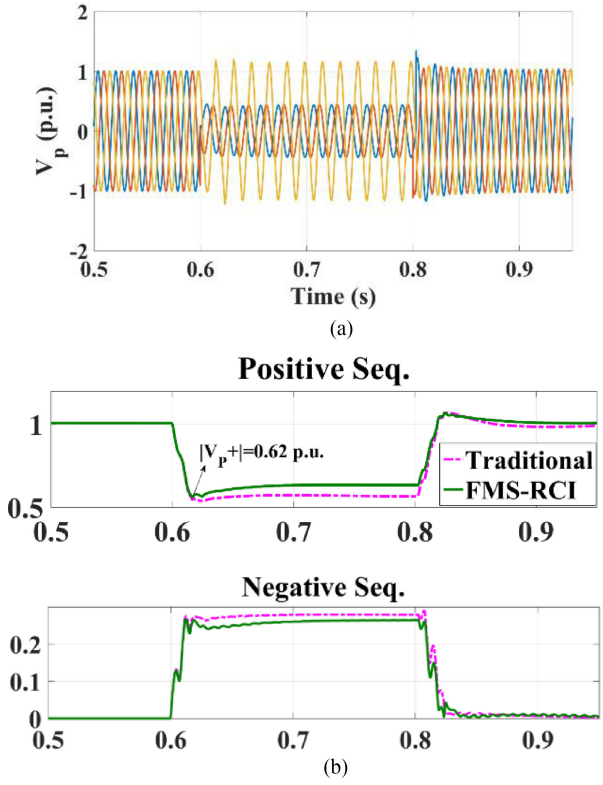

Fig. 8. (a) PCC voltage showing the LVRT performance of the CI-DG unit when employing FMS-RCI. (b) PCC voltage components for the traditional RCG and the FMS-RCI method.

associated problems are highly dependent on the strength of the ac system. As a measure of the system strength, the short-circuit ratio (SCR) is used in this paper. The SCR is a standard definition to quantify the strength of an ac system as compared to the rating of the connected DG unit [26]. If the ac network impedance at the fundamental frequency is considered as Z_s, and the rated ac voltage and power of the converter are V_{rated} and P_{rated}, respectively, then the SCR is defined as [20]

$$\text{SCR} = \frac{V^2{}_{\text{rated}} / Z_s}{P_{\text{rated}}}. \tag{17}$$

To show the effectiveness of the FMS-RCI method in comparison to the traditional RCG method of (1) and (2), the system performance is monitored under an unbalanced fault when the system is connected to a strong grid with SCR = 5.5. In this test case, the detailed nonlinear model of the CI-DG unit of Fig. 1 is implemented in MATLAB/SIMULINK, and a two-phase-to-ground fault at $t = 0.6$ s occurred on bus2 and lasted for 200 ms. The CI-DG unit with the FMS-RCI remains stable during and after the fault, as shown in Fig. 8(a). The positive and negative components of the PCC voltage for the traditional and FMS-RCI methods are shown in Fig. 8(b).

B. LPF Design for the Positive-Sequence Voltage Extraction

As mentioned in Section II, to improve the stability performance of the system, an LPF is used on the positive-sequence

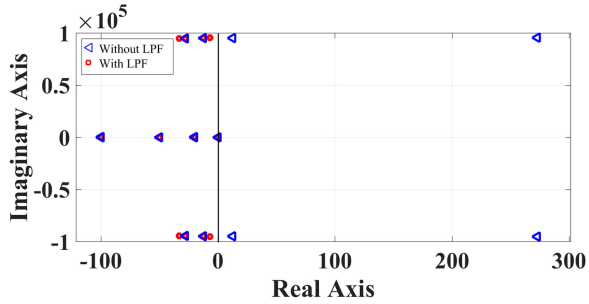

Fig. 9. Dominant poles of the system, before and after applying the LPF to V_{pd}^{+}, when the grid is strong.

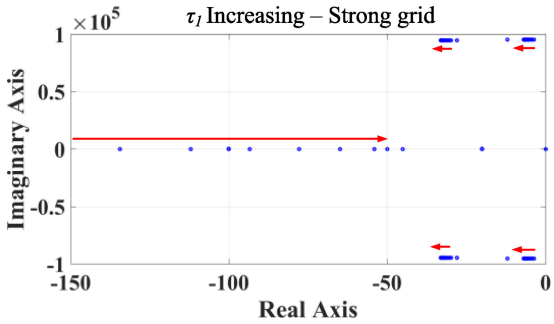

Fig. 10. Eigenvalue locus of the effect of changing the value of τ_1 from $1 \times \tau_i$ to $20 \times \tau_i$ for connection of the DG unit to a strong grid.

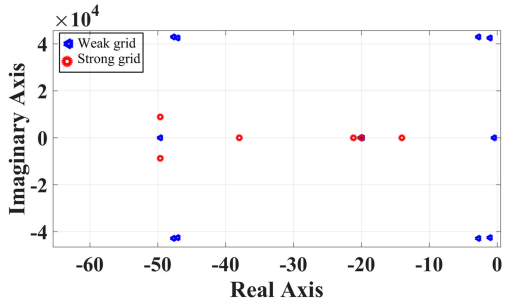

Fig. 11. CI-DG system poles in connection to the strong and weak grids while employing FMS-RCI.

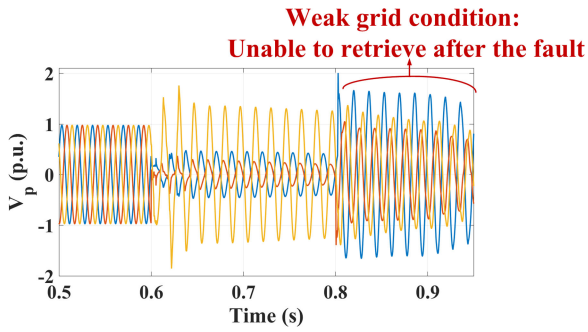

Fig. 12. CI-DG unit performance employing FMS-RCI with the basic control parameter design when the connected grid is weak.

extraction of the PCC voltage in the RCG block, presented in Fig. 4. To illustrate the effectiveness of this method, the most dominant poles of the system before and after applying the LPF are shown in Fig. 9, where the time constant of the filter, τ_1, is set to be three times τ_i [see (5)], which is 3 ms. The system is connected to a strong grid (SCR = 5.5), and all controlling parameters are designed basically. The value of both K^+ and K^- are set to 2.5. Fig. 9 illustrates that the application of this LPF is necessary to employ the FMS-RCI method because there are four unstable poles in the pre-fault linear model of the system when there is no LPF applied on the positive-sequence voltage extraction on the PCC. These eigenvalue analysis results confirmed the time-domain simulation results of Fig. 5, where the system represented instability even for the pre-fault model.

Fig. 10(a) shows the eigenvalue locus when τ_1 changes from $1 \times \tau_i$ to $20 \times \tau_i$ for connection of the DG unit to a strong grid (SCR = 5.5). The linear model represents the complete CI-DG unit with all different controllers; therefore, the eigenvalue analysis includes all interactions among system and control loops. The results show that the design of this LPF does not affect the most dominant oscillatory poles remarkably. But, for $\tau_1 > 10$, it moves one of the real poles toward the origin, which is not desirable. Therefore, for this CI-DG unit, selecting $\tau_1 = 10$ seems reasonable.

V. LVRT Performance Improvement in the Weak Grid Condition

Based on [26], a strong grid is known with the SCR higher than 3, and in a weak grid, the SCR would be lower than 3. Even though the SCR is obtained using steady-state values, it represents a measure of how bus voltages are affected during the dynamic system events [27]. Therefore, in the next step, the performance of the FMS-RCI strategy is studied with the consideration of different grid strengths. To illustrate the importance of this study, the same CI-DG unit is connected to a weak grid with SCR = 1.5, and the same fault scenario of Section IV-A is studied.

Fig. 11 presents the LVRT performance of the CI-DG unit employing the FMS-RCI method with both K^+ and K^- set on 2.5. Compared to Fig. 8(a), the system is highly unbalanced during the fault, and it is unable to retrieve its balance even after the fault is cleared. Therefore, a detailed study seems to be necessary with the consideration of the grid strength on the performance of the FMS-RCI employing DG units.

A. Re-Designing FMS-RCI Parameters Using the Model-Based Design Method

The obtained detailed multi-stage linear model of the CI-DG system provides the possibility of studying the dynamic behavior of the during- and post-fault stages, separately, while respecting the newly imposed grid codes of the LVRT requirements under an unbalanced fault condition. Also, because the complete linear model of the system considers all of the system controllers (e.g., a current controller, PLL, FMS-RCI reference current generators, feed-forward filters, etc.) in detail, the interactions among them are effectively considered in all small-signal stability analyses, which will be presented in the following sections.

As the first step, the complete system poles are obtained in the post-fault stage for the cases of connection to a strong and weak grid. The results are shown in Fig. 12. It is observed that the system poles in connection to a weak grid are remarkably placed

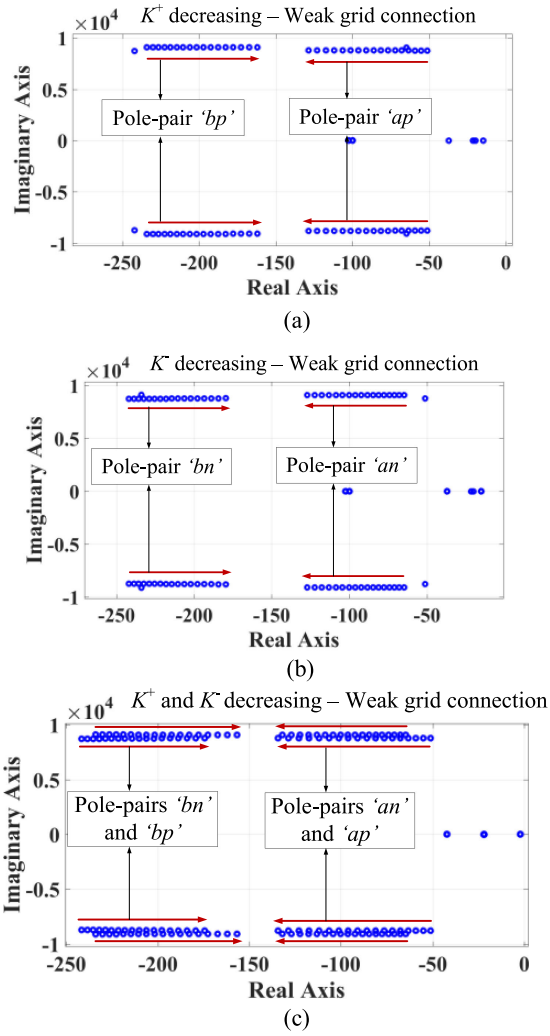

Fig. 13. Eigenvalue locus showing the effect of changing the FMS-RCI parameters when (a) only K^+ is changing, (b) only K^- is changing, and (c) both parameters are changing simultaneously.

closer to the imaginary axis, which represents lower damping in system performance in the case of disturbances.

To start with the model-based design method, first, the effect of changing the FMS-RCI parameters on the stability of the CI-DG unit in connection to a weak grid is studied. Fig. 13 demonstrates that there are two dominant pole pairs connected to each FMS-RCI parameter. For K^+, these pole pairs are labeled by *ap* and *bp* in Fig. 13(a), in which the eigenvalue locus of the most dominant poles of the system is shown when only the value of K^+ is changed from 2.5 to 1, while K^- is kept unchanged on 2.5. Fig. 13(b) also illustrates the other two pole pairs labeled by *an* and *bn* and their trajectory when only K^- is changed from 2.5 to 1, while K^+ is kept unchanged on 2.5. Finally, Fig. 13(c) demonstrates the eigenvalue locus of the most dominant poles of the complete system model when the values of both K^+ and K^- are changed simultaneously from 2.5 to 1. This figure shows that by decreasing the FMS-RCI controlling parameters, there are two pole pairs (already known as *ap* and *an*) moving away from the imaginary axis toward left, while the other pairs (*bp* and *bn*) move toward the imaginary axis.

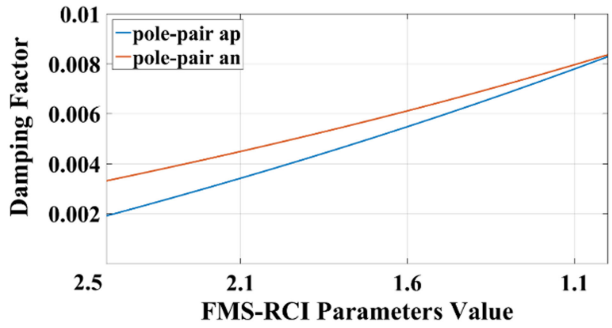

Fig. 14. Damping factor of the pole pairs *an* and *ap* while decreasing the values FMS-RCI parameters K^+ and K^- for the DF stage.

Further studies showed that by decreasing the value of K^+ and K^- lower than 0.3, the *bn* and *bp* pole pairs would pass *an* and *ap* toward the right, which is not desirable. These results reveal that the suggested constant values for K^+ and K^- in [21] are not the most accurate ones considering the stability performance of the system during unbalanced grid condition. Especially, when the connected grid is not strong enough, the selection of these control coefficients should be done more carefully.

The damping factor ξ represents the rate of decay in the amplitude of oscillations. For an oscillatory mode represented by a complex eigenvalue $\sigma \pm j\omega$, the damping factor is defined as

$$\xi = \frac{-\sigma}{\sqrt{\sigma^2 + \omega^2}}. \tag{18}$$

Calculating the damping factor of the mentioned pole pairs shows that selecting the proposed FMS-RCI parameters can considerably increase the damping factor of these dominant modes, which results in an improved transient response of the system. Fig. 14 shows how the damping factor of the mentioned pole pairs *an* and *ap* are increased when the value of K^+ and K^- is changed from 2.5 to 1.

As demonstrated, the value of ξ for the *ap* and *an* pole pairs is increased to four and three times its initial value, respectively. This means that the oscillations related to these poles will be damped four and three times faster than before. On the other hand, since lower K^+ and K^- means that the DG unit is receiving lower voltage support during the fault [see (3) and (4)], they should be kept at an optimum value, which delivers higher damping factor but at the same time prevents the PCC voltage from deep sag during the fault and, finally can present a successful LVRT.

One important point about these findings is that they show how changing the values of K^+ and K^- affect the transient stability of the system, while all other system dynamics are taken into account. Therefore, the initial design of the FMS-RCI parameters can be modified based on this eigenvalue analysis results to guarantee a stable performance of the CI-DG unit in connection to a weak grid. As mentioned before, the initial design of all controller compensators is done basically based on satisfying a stable phase and gain margin using the Bode plot. Besides, because the FMS-RCI parameters are effective when

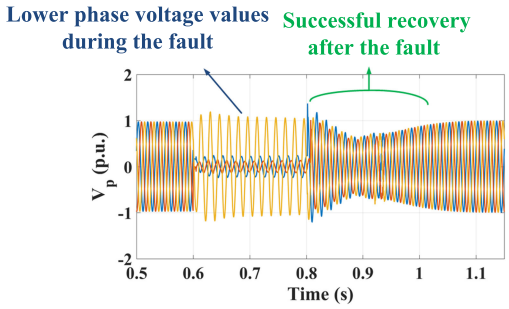

Fig. 15. CI-DG unit performance employing FMS-RCI with $K^+ = K^- = 1$ when the connected grid is weak.

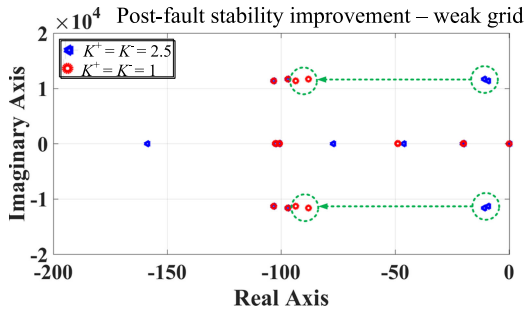

Fig. 16. Dominant poles of the post-fault system model showing the effect of improved FMS-RCI parameters.

TABLE II
DAMPING FACTOR IMPROVEMENT IN THE DOMINANT POLES OF THE POST-FAULT MODEL

Pole pair 1	ξ_{old}=9.16e-4	ξ_{new}=74e-4	ξ_{new}/ξ_{old} =8.08
Pole pair 2	ξ_{old}=7.98e-4	ξ_{new}=82e-4	ξ_{new}/ξ_{old} =10.27

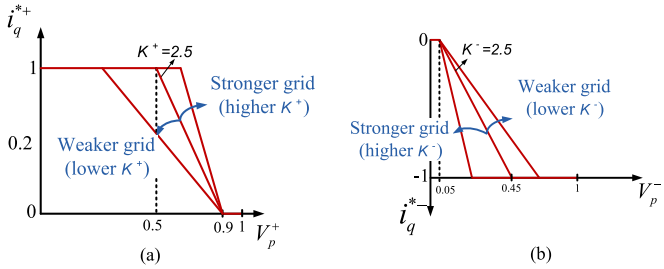

Fig. 17. Modified selection of the FMS-RCI parameters based on the grid strength for (a) positive sequence, and (b) negative sequence of the reactive current injection.

the system is in eq_2^+ or eq_2^-, the above-presented eigenvalue locus is obtained using the during-fault stage model. The results for the post-fault stage are also obtained, which revealed similar trends. However, due to the space limitation, only the results for the during-fault model are shown in this step. Therefore, this method suggests a higher stability margin for the case of a DG unit connected to a weak grid.

The other remarkable point about this model-based compensator design method is that, although the results are obtained using the small-signal stability analysis, they are applicable in the large-signal stability analysis of the same system. To verify this statement, the obtained new values for K^+ and K^- (i.e., K^+ and K^- set to 1) are used in the same detailed nonlinear model of the system when the connected grid is weak with SCR $= 1.5$. The result is shown in Fig. 15. Comparing this with Fig. 11 reveals that by decreasing the value of FMS-RCI parameters, the large-signal stability of the system is also improved. As shown, the system could retrieve its stable and balanced operation after fault clearance, which yields reliable system operation. The system is returned to the pre-fault steady state around 200 ms after the fault clearance. These results demonstrate that the proposed model-based method can improve the overall LVRT performance of the system when the connected grid is not strong enough.

To study more details on the stability improvement after fault clearance, the eigenvalues for the post-fault model are obtained for two different operating points: first, with the initial values of $K^+ = K^- = 2.5$, and, second, with the suggested FMS-RCI parameters obtained in the small-signal stability analysis, as shown in Fig. 16. There are two pairs of dominant poles, encircled in Fig. 16, which moved toward left, representing higher damping factor in the post-fault stage. This result verifies what is observed in Fig. 15 from the time-domain simulation study.

Table II shows how the damping factor of the demonstrated poles in Fig. 16 are increased in the post-fault stage, which justifies the improved transient behavior of the system in providing a successful LVRT with the proposed model-based design of the FMS-RCI parameters.

These results represent a significant improvement in satisfying the LVRT requirements while employing the FMS-RCI in a CI-DG unit connected to a weak grid. Due to the direct interconnection with power grids, CI-DG units are particularly sensitive to non-ideal grid conditions, e.g., grid impedance, background harmonics, and grid voltage sags or swells, which often occur in weak grids. Hence, the stability and power quality of the GCC will be significantly influenced. This could become worse as the penetration level becomes higher increasingly, which is common in the recent power grids. However, this study showed that reconfiguring the FMS-RCI controlling parameters provides a higher range of certainty for the system when encounters a grid fault to satisfy the new grid code requirements, during and after the fault.

As mentioned in (17), the value of the SCR is inversely related to the ac network impedance at the fundamental frequency (Z_s). Therefore, since $\Delta V_p^+ \propto i_q^+ Z_s$, higher Z_s which means lower SCR should be followed by lower i_q^+ to keep the PCC voltage balanced on 1.0 p.u., which represents lower K^+. The same discussion applies to the negative-sequence reactive current injection. This fact confirms the obtained results of this paper.

Fig. 17 illustrates the modified diagrams of Fig. 3 based on the small-signal analysis and the time-domain simulation results obtained in this section. As presented, for connection to a weaker grid, lower FMS-RCI parameters can satisfy the LVRT

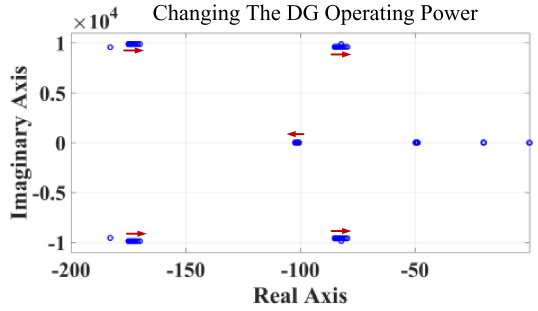

Fig. 18. Eigenvalue locus showing the effect of the pre-fault state on the during-fault stability of the system by changing the DG operating power from very small load to full load.

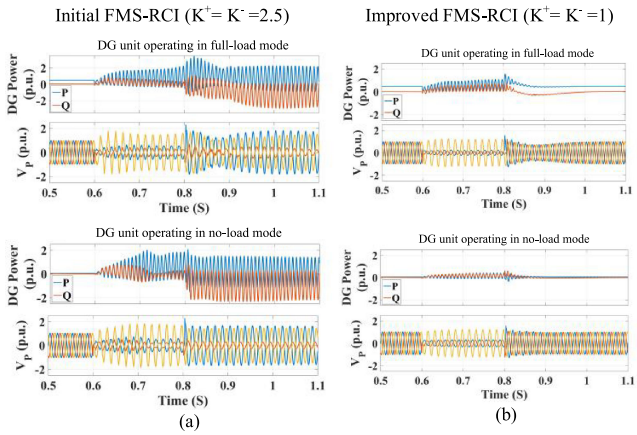

Fig. 19. Time-domain simulation results showing the effect of pre-fault state on the LVRT performance of the DG unit in connection to the weak grid when employing the FMS-RCI method with (a) the initial design and (b) the proposed design.

requirements of the grid code and, at the same time, keep the system stable during and after the fault.

Besides, as demonstrated in Fig. 2(a), for any voltage drop lower than 45% to zero, which may last for 150 ms, the grid code requires the DG unit to stay connected and return to the normal condition up to 1500 ms after the fault. All of these constraints are considered and satisfied in the studied cases of this paper.

As an overall summary, it is demonstrated that changing the values of K^+ and K^- affects the transient stability of the whole system. The results show that in the case of a weak grid condition, reducing the values of K^+ and K^- guarantees a stable performance of the CI-DG unit under a grid fault. Besides, the proposed model-based compensator design method can also improve the large-signal stability of the system and enhance its post-fault stability performance.

B. Effect of the Pre-Fault Stage on the LVRT Performance of the DG Unit

In this section, the effect of the pre-fault stage on the LVRT performance of the DG unit during the fault is studied. The pre-fault stage of the DG unit is changed by changing its operating power in a wide range (from small no-load to full-load), and the effect of this starting point on the dynamic performance of the during-fault stage in connection to the weak grid is studied. In the previous test cases, the operating power of the DG unit was set to the full load. Fig. 18 shows the eigenvalue locus of system dominant poles with the consideration of all system and controllers dynamics. The DG operating power is changed from 0.1 p.u. to 1 p.u. of the DG unit rating, while the connected grid is weak with SCR $= 1.5$ and the FMS-RCI parameters are set to 1, according to the results of Section V-A. As demonstrated, changes in the pre-fault state have a small effect on the transient stability of the system during the fault when the proposed augmented design method for the FMS-RCI parameters is utilized. However, since by increasing the operating power of the DG unit, its strength is accelerating in comparison to the utility grid, by considering the definition of the SCR, this approach can also be seen as reducing the system SCR. Hence, the illustrated trajectory of the affected dominant poles toward the RHP is also justified, which represents lower stability margin for the whole system. Therefore, according to the proposed method of Section V-A, in case of a failure in the LVRT when the DG unit operating power is increased, selecting lower FMS-RCI parameters is suggested to guarantee a successful LVRT. It is worth mentioning that the same eigenvalue locus trend is also observed for the case of FMS-RCI parameters set to 2.5, in which the DG unit is unable to retrieve to the stable operation after the fault. The results reveal that the optimal selection of the FMS-RCI parameters with the consideration of the grid strength is considerably more effective on presenting a stable and successful LVRT performance of the system compared to the effect of the pre-fault state of the DG unit. However, it is inferred that in the case of DG unit operating in lower load condition, higher values for the FMS-RCI parameters can be selected to improve the voltage support during the fault.

To validate the results of Fig. 18, the time-domain simulation results of the system under different pre-fault states in connection to a weak grid are obtained. The results are shown in Fig. 19, where the superior effect of the proposed FMS-RCI parameters selection compared to the pre-fault state of the DG unit is demonstrated.

C. Re-Designing Other Compensators With the Initial FMS-RCI Parameters Using the Model-Based Design Method

Although selecting lower K^+ and K^- values could improve the small- and large-signal stability performance of the CI-DG unit under an unbalanced fault condition, it represents a lower injection of the positive and negative reactive current components to the system during the fault. Hence, the voltage support characteristic of the FMS-RCI strategy will not be as effective as before.

To keep the values of K^+ and K^- higher but still have a stable and balanced LVRT operation, another study is carried out to investigate the effect of other compensators parameters on the stability of the complete CI-DG unit system in weak grid condition. In this study, the eigenvalue analysis is employed again to investigate the effect of changing the proportional and integral gains (i.e., K_p and K_i, respectively) of the PLL and

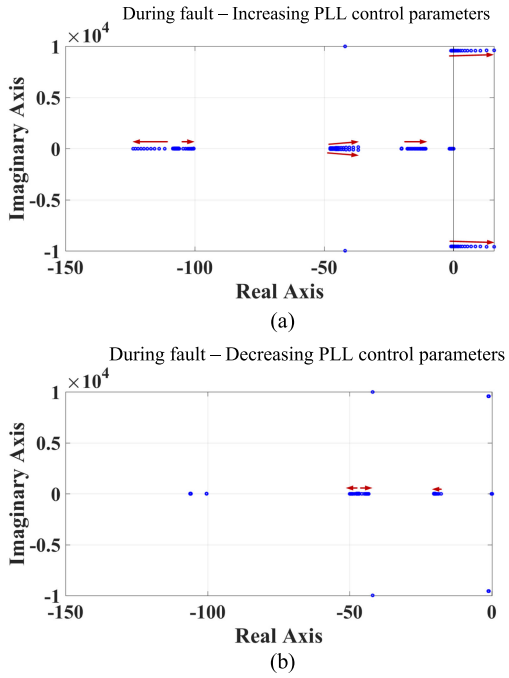

Fig. 20. Eigenvalue locus showing the effect of changing the PLL controller PI gains with the initial FMS-RCI parameters when (a) increasing and (b) decreasing the PLL gains.

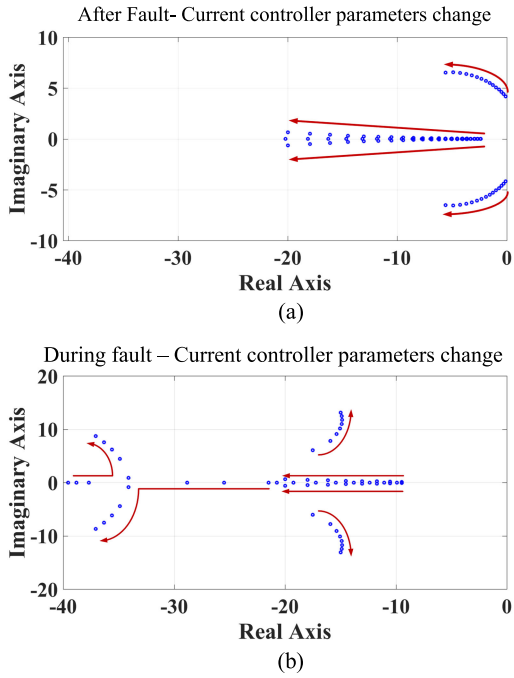

Fig. 21. Eigenvalue locus showing the effect of changing the current controller PI gains with the initial FMS-RCI parameters in (a) post-fault stage and (b) during-fault stage.

the current controller compensators. The initial design of these compensators is obtained based on the methods presented in [25]. For the PLL, the second-harmonic rejection along with an acceptable bandwidth and damping factor is considered. For the current controller, the PI gains are designed to provide a dc reference tracking in the *dq* frame by considering the pole-zero cancellation in the open-loop transfer function.

To employ the model-based parameter design for each compensator, its PI gains are changed, and the related eigenvalue locus is obtained. In the first step, the effect of changing the PLL control parameters is studied, while the system is connected to a weak grid (SCR $= 1.5$) and $K^+ = K^- = 2.5$. The results for the during-fault model are shown in Fig. 20. It is observed that changing the PLL compensator gains from their initial design aggravates the stability criteria [see Fig. 20(a)] or does not change it remarkably [see Fig. 20(b)]. Because changing the PLL gains does not improve the small-signal stability of the system, in the next studies, the value of the PLL control parameters is kept on their initially designed values.

In the next step, the PI gains of the current controller are changed in both during- and post-fault stages of the linear models. The eigenvalue locus is shown in Fig. 21. As illustrated, by decreasing the integrator gain of the current controller, K_i, to 10% of its initial value, while the proportional gain, K_p, is kept constant, the most dominant poles in both stages move away from the imaginary axis toward left. It represents higher damping factor related to these modes and, so, higher relative stability in the system. Changing K_p individually or at the same time with K_i made some of the most dominant poles move toward the right; therefore, this value is kept unchanged. These results revealed that by reducing the value of K_i in the current controller from its initially designed value and keeping the FMS-RCI parameters high on 2, the relative stability of the CI-DG unit in connection to a weak grid is improved for both during- and after-fault stages.

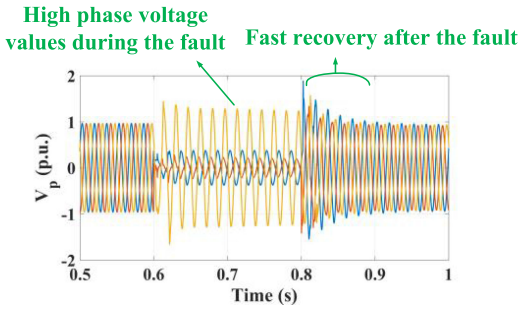

Fig. 22. CI-DG unit performance employing FMS-RCI with $K^+ = K^- = 2$ and current controller K_i reduced by 10% when the connected grid is weak.

To verify the abovementioned results, the previous scenario is carried out in the detailed nonlinear model of the system. The DG unit is connected to a weak grid of SCR $= 1.5$, and the same unbalanced fault occurs on bus2. K^+ and K^- are set to 2; the current controller K_i is reduced by 10%. Fig. 22 shows the results of the PCC voltage LVRT performance. Compared to Fig. 11, it reveals that the transient stability characteristic of the system is improved, and it could retrieve to the balanced and stable operation in less than 100 ms, while the injection of the reactive current components is kept high during the fault. This

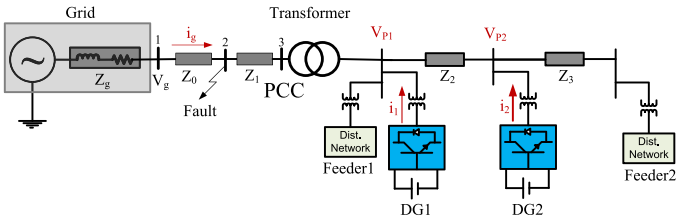

Fig. 23. Two-DG system under study.

fact is also evident by comparing Figs. 15 and 22 for the phase voltage values during the fault.

The results of this section are another verification of the capability of the proposed model-based design to be valid for both small-signal and transient stability improvement of the system considering LVRT requirements. The main advantage of the proposed method of this section is that by choosing higher FMS-RCI parameters and reducing the current controller PI parameters, the PCC voltage receives higher support during the unbalanced fault and, at the same time, the system satisfies the LVRT requirements and rides through the fault. It is worth mentioning again that, because the linearized models in all three stages are obtained considering all controllers and filters, the results of the eigenvalue analyses in all studies of this paper include the interactions among all of these units. Therefore, unlike the conventional individual controller design approach, the proposed augmented model-based design approach accounts for the interactions among different controllers, grid dynamics, and parameters. Also, it could optimize the dynamic performance of the whole GCC system.

VI. Multi-DG System

To study the application of the findings of the previous sections to different systems, a more complicated medium-voltage distribution system including some local loads and two CI-DG units, shown in Fig. 23, is employed and used for nonlinear time-domain simulation studies. The loads are represented by parallel RL elements. Both DG units are equipped with the FMS-RCI method to support the LVRT requirements.

To study the performance of this multi-DG system while employing the FMS-RCI method, two scenarios are considered in this paper: 1) one-DG system expansion; and 2) two-DG system planning. Each scenario is thoroughly studied in the next subsection.

A. Scenario 1: One-DG System Expansion

In the first scenario, an existing system with one CI-DG unit is supposed to be extended to the two-DG system of Fig. 23. In this case, the rating of the first DG is already determined. As a case study, the second DG is selected to be with the same rating as the first DG, and the total connected load is 1 p.u. As a reasonable supposition, the line impedance between two DGs is around 20% of the grid impedance. Therefore, bus3 can still be considered as the PCC for both DGs, and so, the initial grid strength or the SCR of this system will be almost half of

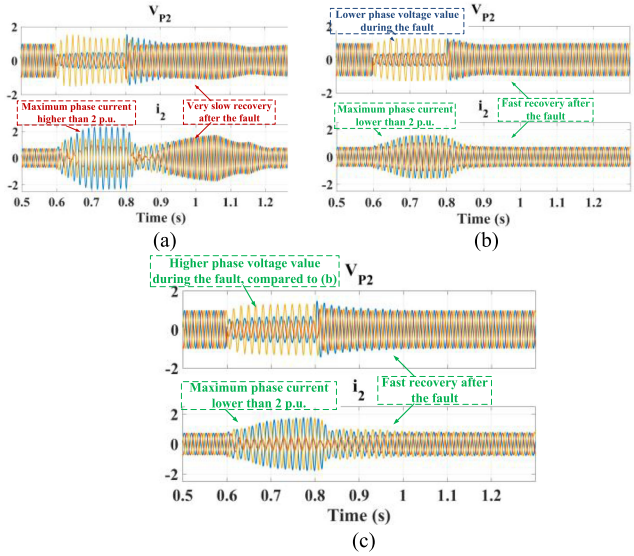

Fig. 24. Effect of selecting improved controlling parameters in scenario #1 of the two-DG system when connected to a weak grid. (a) With $K^+ = K^- = 2.5$ and initial compensator design. (b) With $K^+ = K^- = 1$ and initial compensator design. (c) With $K^+ = K^- = 2$ and current controllers K_i parameter reduced by 10%.

what it initially was in the one-DG unit system of Fig. 1, i.e., SCR $\approx$ 3. By referring to the results of Section V-A, it seems reasonable to select the initial values of K^+ and K^- lower than 2.5 for both DGs in this scenario. Hence, during the unbalanced condition, each DG will support the PCC by injecting its ratio of the positive and negative reactive current components. This hypothesis is proved and shown in Fig. 24, where changing K^+ and K^- values from 2.5 [see Fig. 24(a)] to 1 [see Fig. 24(b)] could improve the system performance during and after the fault, whereas the other controllers parameters are kept intact. In Fig. 24(a), the settling time after the fault clearance is almost 400 ms, and the maximum phase current during the fault is high, which may activate the protection relays. For space saving, only the signals of DG2 are shown in Fig. 24 because the signals of DG1 also represent the similar characteristics.

To show the effectiveness of the proposed method of Section V-B, in the next test, the K^+, and K^- values are set higher (to 2), but the value of the integrator gain of the current controller of both DGs is reduced to 10% of its initial value. The results are presented in Fig. 24(c), where the performance improvement is clear compared to Fig. 24(a).

B. Scenario 2: Two-DG System Planning

In the second scenario, a two-DG system should be designed, and the proper rating for both DGs can be defined. By having the same grid with the initially known short-circuit characteristic, an economical selection for the DG units with the same 1 p.u. load is to have each DG unit with the rating as half of what it was in the first scenario, i.e., 2.5 MVA. Therefore, the grid strength will initially be high with SCR = 5. In this case, with both DGs equipped with the FMS-RCI method, the initial selection of $K^+ = K^- = 2.5$ represents an acceptable LVRT performance for the two-DG system. However, when the con-

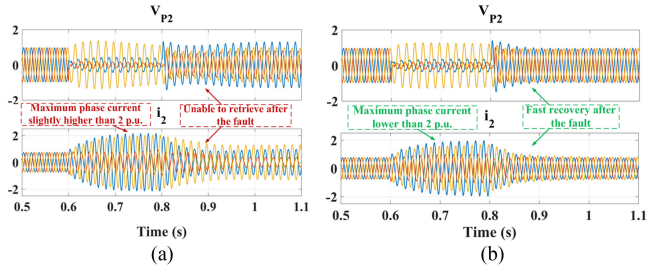

Fig. 25. Effect of selecting improved controlling parameters in scenario #2 of the two-DG system when connected to a weak grid. (a) With $K^+ = K^- = 2.5$ and initial compensator design. (b) With $K^+ = K^- = 2$ and current controllers K_i parameter reduced by 10%.

Fig. 26. View of the experimental test setup.

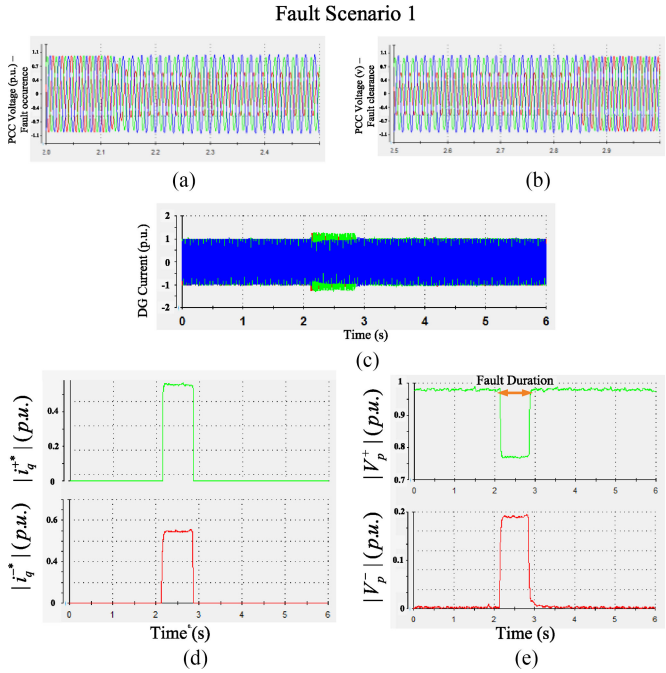

Fig. 27. Experimental results for Fault Scenario 1 when $K^+ = K^- = 2.5$. (a) PCC three-phase voltage on fault occurrence. (b) PCC three-phase voltage on fault clearance. (c) DG current (i_1). (d) Injected reactive reference current values. (e) PCC voltage in positive/negative *dq* frames.

nected grid is weak with SCR = 2, both DGs will be unable to retrieve their balanced and stable operation after being subjected to the unbalanced fault. This event can be seen in Fig. 25(a). As a remedy, the proposed methodology of Section V-B is applied to the system controllers. The results of Fig. 25(b) illustrate the effectiveness of this method in improving the large-signal stability of the tow-DG system in connection to the weak grid.

VII. Experimental Results

The results of the time-domain and the state-space stability analyses are also validated using a scaled-down 1.0-kVA, 208-V (line-to-line), three-phase, 60-Hz, grid-connected VSC laboratory prototype, as shown in Fig. 26. The scaled-down experimental test setup is widely used in the power system studies [28]–[30]. The key components for the laboratory setup are a dSPACE DS1104 real-time control systems, a three-leg VSC (Semistack intelligent power modules, each includes gate drives, six insulated gate bipolar transistors, and protection circuit), 60-Hz three phase grid, interfacing transformers, and sensor boxes to sample voltages and currents. The converter is interfaced to a control card using an interfacing circuit. The pulsewidth modulation and the converter controllers are implemented on the dSPACE control card supported with a coprocessor structure for switching signal generation. The grid stiffness is changed by connecting series inductors to the ac grid so that the SCR of the studied system can be varied.

For the strong grid condition, the SCR is considered 6.6, and for the weak grid condition, the SCR is set to be 2.1. To study the effectiveness of the proposed methods in Sections V-A and V-B, three fault scenarios are studied in the following subsections.

1) Fault Scenario 1: The DG unit is connected to a strong grid with SCR = 8, and it encounters a short-term unbalanced one-phase to ground fault.
2) Fault Scenario 2: The DG unit is connected to a weak grid with SCR = 1, and it encounters a short-term unbalanced one-phase to ground fault.
3) Fault Scenario 3: The DG unit is connected to a weak grid with SCR = 1, and it encounters a short-term unbalanced two-phase to ground fault.
4) Fault Scenario 4: The DG unit is connected to a weak grid with SCR = 1, and it encounters a short-term unbalanced one-phase to ground fault when it is operating under different pre-fault status.

A. Fault Scenario 1

In this test case, the DG unit is connected to the strong grid and the FMS-RCI is adopted with $K^+ = K^- = 2.5$. Fig. 27(a) and (b) show the three-phase PCC voltage when the system encounters an unbalanced one-phase-to-ground fault on the line between the DG unit and the grid. As shown in Fig. 27(c), the DG unit could ride through the fault and remain connected to the grid, which represents a successful LVRT based on the grid code requirements. The PCC voltage components are shown in Fig. 27(e) illustrating that in this fault scenario, the injection of the reactive current components will be obtained based on eq_2^+ and eq_2^- of (3) and (4). According to Fig. 27(c), the value of the DG unit current stayed below the defined thermal limit (i.e.,

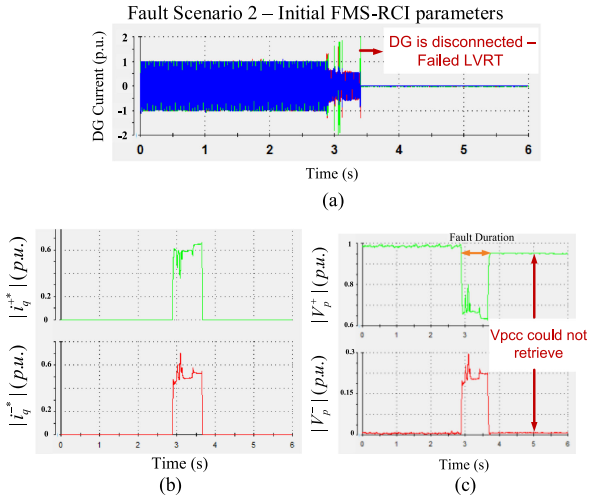

Fig. 28. Experimental results for Fault Scenario 2 when $K^+ = K^- = 2.5$. (a) DG current (i_1). (b) Injected reactive reference current values. (c) PCC voltage in positive/negative *dq* frames.

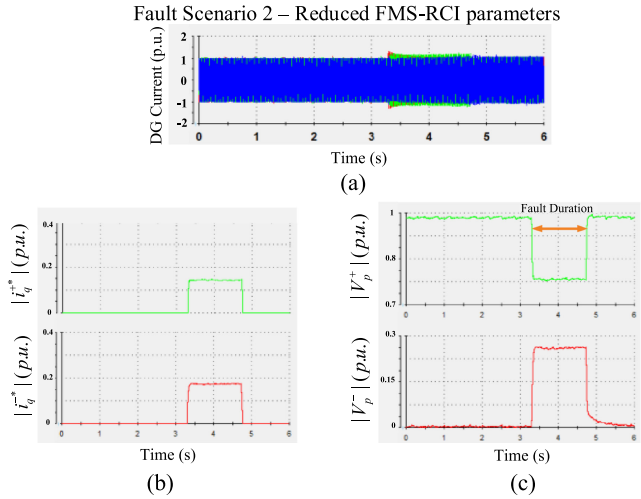

Fig. 29. Experimental results for the Fault Scenario 2 when $K^+ = K^- = 0.7$. (a) DG current (i_1). (b) Injected reference current values. (c) PCC voltage in positive/negative *dq* frames.

1.0 p.u.) during the fault, which means the injection of the active current can be obtained based on (1) during this time.

B. Fault Scenario 2

In this test case, the CI-DG unit is connected to the weak grid with SCR = 1, and the system encountered an unbalanced one-phase-to-ground fault on the line between the DG unit and the grid. The effectiveness of the proposed model-based methods of Section V-A and B are studied in three subsections as follows.

1) FMS-RCI Gain Effect: In the first step, the FMS-RCI parameters are set on $K^+ = K^- = 2.5$. Fig. 28(a) shows that the value of the converter current has remained below the thermal limit (i.e., 1.0 p.u.) during the fault, which allows the injection of the reactive current components based on eq_2^+ and eq_2^- of (3) and (4) and injection of the active current based on (1). However, after the fault clearance, the converter cannot retrieve to its previous stable operation, and the value of its current exceeds the determined thermal limit, which causes the disconnection of the DG unit and failure of the LVRT.

Therefore, to prevent the DG unit disconnection and based on the results of Section V-A, the values of K^+ and K^- are reduced to 0.7, and the same fault scenario of Fig. 28 is studied. As demonstrated in Fig. 29, the system represented a successful LVRT performance and could successfully retrieve stable operation after the unbalance fault. These results verify the findings of Figs. 13 and 15. Considering the value of the converter current, shown in Fig. 29(a), the determined thermal limit of the DG unit is respected during the fault, and the DG unit remained connected to the grid, which represents a successful LVRT.

2) PLL Gain Effect: To investigate the results of Section V-B, first, the effect of changing the PLL gains in the experimental test setup is studied, while setting the FMS-RCI gains back to their original values (i.e., $K^+ = K^- = 2.5$). The initial designed value for K_{p_PLL} is 5 and K_{i_PLL} is assumed

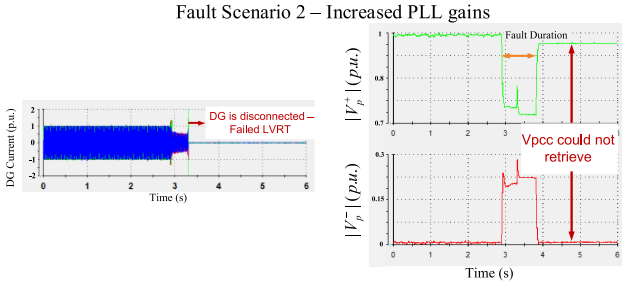

Fig. 30. Experimental results for Fault Scenario 2 when $K^+ = K^- = 2.5$ and the PLL gains are increased.

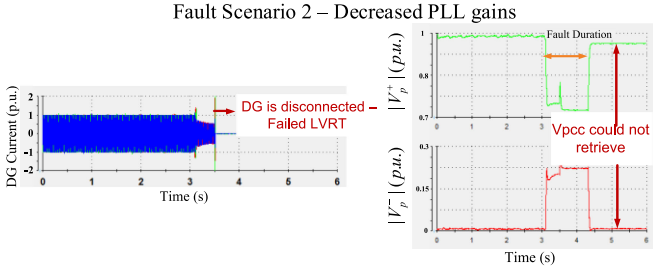

Fig. 31. Experimental results for Fault Scenario 2 when $K^+ = K^- = 2.5$ and the PLL gains are decreased.

to be $5 \times K_{p\_\mathrm{PLL}}$ [20]. In the first test, the value of K_{p_PLL} is increased, and the same fault scenario is studied.

Fig. 30 shows the result for the case of $K_{p\_\mathrm{PLL}} = 80$. The next two test cases are performed when K_{p_PLL} is reduced to 0.25 under the same fault condition. In the first case, the value of FMS-RCI gains is set to 2.5 (see Fig. 31), and in the second one, the value of FMS-RCI gains is reduced to 2 (see Fig. 32). All cases demonstrate the failure of the DG unit in satisfying

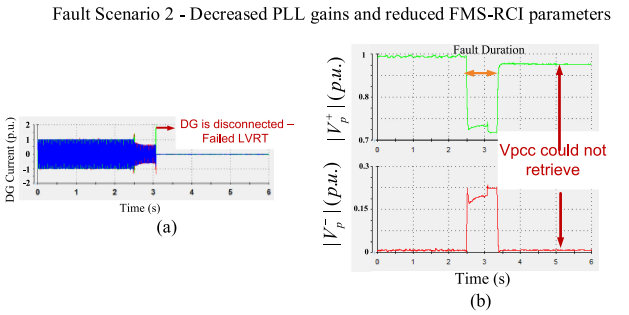

Fig. 32. Experimental results for Fault Scenario 2 when $K^+ = K^- = 2$ and the PLL gains are decreased.

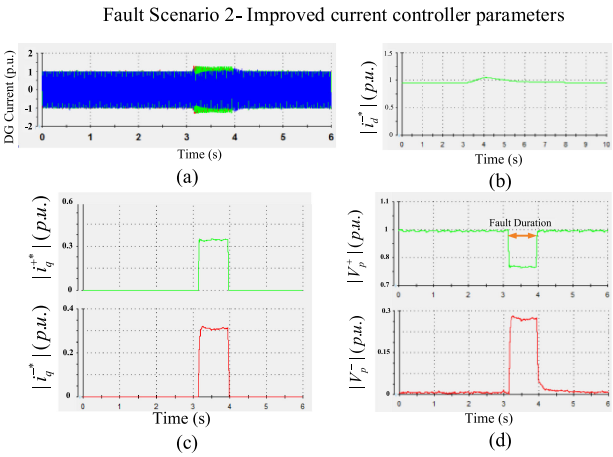

Fig. 33. Experimental results for Fault Scenario 2 with improved current controller gains design when $K^+ = K^- = 1.5$. (a) DG current (i_1). (b) Injected active current. (c) Injected reference reactive current values. (d) PCC voltage in positive/negative *dq* frames.

the LVRT requirements, which verifies the eigenvalue analysis results of Fig. 20.

3) Current Controller Gain Effect With Higher Voltage Support: To validate the findings of Section V-B, in the next test case, the FMS-RCI parameter value is increased to 1.5 to provide higher voltage support in the case of the weak grid condition, compared to the test case of Section VII-B1. Besides, to prevent the protection system from disconnecting the CI-DG unit and based on the findings of Fig. 21, the value of the initially designed current controller integrator gain, K_i, is reduced by 10%. The system experienced Fault Scenario 2, and the results are shown in Fig. 33. The DG unit remained connected to the grid and represented a successful LVRT operation. Compared to Fig. 29(b), the DG unit is generating higher reactive current values during the fault, while still respecting the thermal limit [see Fig. 33(a) and (b)], which results in an improved PCC voltage support.

C. Fault Scenario 3

To investigate the effectiveness of the proposed methods under a different voltage unbalance ratio, a two-phase-to-ground

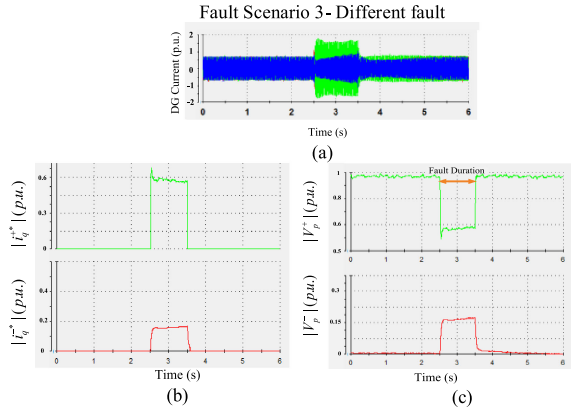

Fig. 34. Experimental results for Fault Scenario 3 with improved current controller gains design when $K^+ = K^- = 1.5$. (a) DG current (i_1). (b) Injected reference reactive current values. (c) PCC voltage in positive/negative *dq* frames.

fault is studied in this section. The PCC voltage components are shown in Fig. 34(c). By comparing these results with Fig. 33(d), a deeper voltage drop on the positive sequence and lower voltage unbalance with lower negative-sequence value can be observed. The same control method of Section VII-B3 with the improved current controller parameters and $K^+ = K^- = 1.5$ is used in this study. The results of Fig. 34 reveal the effectiveness of the proposed methods in delivering a successful LVRT performance.

D. Fault Scenario 4

To investigate the results of Section V-B on the study of the effect of the pre-fault status of the DG unit of the LVRT performance of the system, the pre-fault operating power of the CI-DG unit is changed, and the unit is encountered a short-term unbalanced one-phase-to-ground fault.

The results are shown in Fig. 35. First, the operating power of the DG unit is reduced to half load, which, based on the concept of SCR, can be inferred as increasing the system SCR. In this test, the value of the FMS-RCI parameters is set to 2. As presented in Fig. 35(a) and (b), the system could ride through the fault and represent a successful LVRT. By comparing these results with the results of Fig. 28, it can be seen that the system is performing more stably and can provide the PCC voltage with higher voltage support under the same fault condition.

In the next test, the operating power of the DG unit is reduced to 80%, under the same fault scenario. As presented in Fig. 35(c) and (d), the system could not demonstrate a successful LVRT, and the DG unit is disconnected from the grid. These results verify the eigenvalue analysis results of Section V-B.

VIII. Discussion

This paper presented how the grid strength affects the initial standard design of different control loops. This standard design is based on the assumption that these loops can be designed individually without the consideration of their coupling on each other [25]. This assumption is valid in the case of connection of

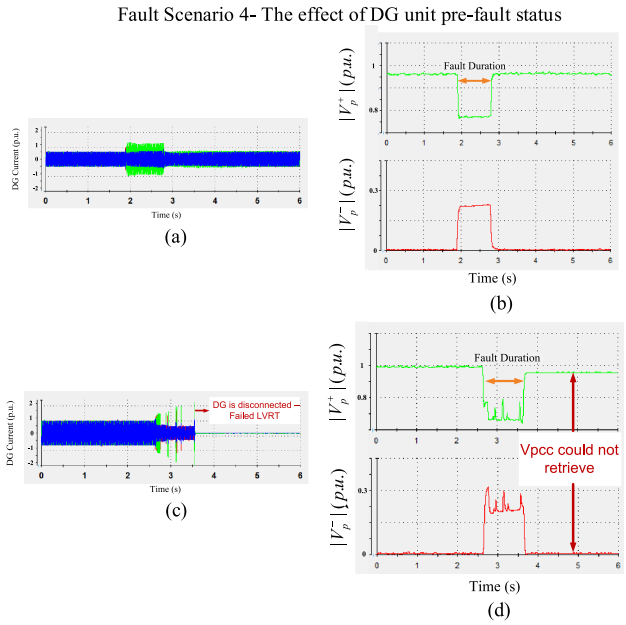

Fig. 35. Experimental results for Fault Scenario 4 with different pre-fault states when $K^+ = K^- = 2$. (a) DG current (i_1) when the DG unit is operating under the half-load condition. (b) PCC voltage in positive/negative *dq* frames) when the DG unit is operating under the half-load condition. (c) DG current (i_1) when the DG unit is operating under the 80%-load condition. (d) PCC voltage in positive/negative *dq* frames) when the DG unit is operating under the 80%-load condition.

a DG unit to a strong grid (i.e., with SCR $>>$ 3). However, when the connected grid is not strong, the coupling among different control loops (e.g., the current controller, voltage controller, PLL, etc.) cannot be ignored anymore. These control loops affect each other and need comprehensive analysis and design methods. Therefore, the initial individual design of the control loops may not be effective under different circumstances. This fact is studied in this paper under the unbalance fault condition, where the DG unit is also supposed to provide a successful LVRT based on the grid code requirements. Based on the comprehensive studies and detailed model analysis, some obtained values are provided to show the main contributions of the proposed analysis and design methods in this paper. In other words, the provided values are some examples obtained by the detailed analysis and design methods proposed in this paper based on the characteristics of the studied system. The key contribution here is to demonstrate how to modify the initial control parameters by the proposed comprehensive design method to obtain a successful LVRT performance, flexible grid support capability, and dynamic response and stability performance improvement under weak grid and unbalanced conditions.

Therefore, according to the above discussion, this paper has proposed the augmented control parameter design, which is obtained based on the small-signal stability analysis of the comprehensive linearized model of the system, in which all system parameters and the control loops are considered at the same time in one model. In this way, all hidden feedbacks and couplings among these loops are thoroughly considered in the system performance analysis. However, the exact quantities will obviously be different based on different system specifications such as higher or lower system SCR, different DG unit ratings, line impedances, the location of the fault, the severity of the faults that are required to be ridden through by a specific grid code, etc. As it is also demonstrated in Fig. 16, this paper has been able to propose more details and the main idea on how to modify the initial FMS-RCI parameters mentioned in the VDE German grid code [9], based on different grid strengths to increase the chance of having a successful LVRT performance by the GCC-based DG unit. The most important contribution of this study is proposing the augmented model-based design for all control loops, based on the small-signal stability analysis on the detailed comprehensive linearized model of the system. Therefore, the system designers would be able to keep the FMS-RCI parameters at higher values (imposed by specific grid codes) by modifying the standard control parameters of the DG unit. This will allow DG units to comply with the strict requirements of specific grid codes on higher voltage support capability during the fault. Therefore, the DG unit will show much better performance in vulnerable grid conditions (e.g., weak grids) under severe grid faults (e.g., severe low voltages and unbalanced faults) and in compliance with strict grid code requirements (e.g., flexible multi-sequence voltage support) by just proper modifications in its control design using the proposed methods in this paper.

IX. Conclusion

A three-stage modeling approach of a CI-DG unit system equipped with an FMS-RCI method is presented in this paper. The small-signal stability analysis is performed on the system dynamic behavior before, during, and after the unbalanced fault and under the weak grid condition. A new and effective model-based controller parameter design method is proposed to maintain the system stability during and after the fault with the consideration of the mutual interaction among different system controllers. The proposed control system design improved the relative stability of the system under the weak grid condition when subjected to an unbalanced fault; at the same time, the amount of the positive and negative components of the injected reactive current during the unbalanced fault follows the grid code requirements. Then, by applying the proposed design of the controller parameters in the nonlinear time-domain model of the system, the large-signal LVRT performance improvement is observed in the CI-DG in connection to a weak grid. Finally, the laboratory experiments validated the accuracy of the developed model and the effectiveness of the proposed strategies.

Appendix

$$A_{1_{(23\times23)}} = \begin{bmatrix} A_{1a_{(12\times12)}} & A_{1b_{(12\times11)}} \\ A_{1c_{(11\times12)}} & A_{1d_{(11\times11)}} \end{bmatrix} \tag{A1}$$

where

$$A_{1a_{(12\times12)}} =$$

	1	2	3	4	5	6	7	8	9	10	11	12
1	$\frac{-R_1-R_0}{L_1+L_0}$	ω_0										
2	$-\omega_0$	$\frac{-R_1-R_0}{L_1+L_0}$										
3			$\frac{-R_1-R_0}{L_1+L_0}$	$-\omega_0$								
4			ω_0	$\frac{-R_1-R_0}{L_1+L_0}$								
5					$\frac{-R_f}{L_f}$					$\frac{K_i}{L_f}$		
6						$\frac{-R_f}{L_f}$				$\frac{K_i}{L_f}$		
7							$\frac{-R_f}{L_f}$				$\frac{K_i}{L_f}$	
8								$\frac{-R_f}{L_f}$			$\frac{K_i}{L_f}$	
9					-1							
10						-1						
11							-1					
12								-1				

(A2)

$$A_{1b_{(12\times11)}} =$$

	1	2	3	4	5	6	7	8	9	10	11
1	i_{gq}^{+}	$\frac{1}{(L_1+L_0)}$									
2	$-i_{gd}^{+}$		$\frac{1}{(L_1+L_0)}$								
3	$-i_{gq}^{-}$			$\frac{1}{(L_1+L_0)}$							
4	i_{gd}^{-}				$\frac{1}{(L_1+L_0)}$						
5	i_{1q}^{+}	$\frac{-1}{L_f}$				$\frac{1}{L_f}$					
6	$-i_{1d}^{+}$		$\frac{-1}{L_f}$				$\frac{1}{L_f}$				
7	$-i_{1q}^{-}$			$\frac{-1}{L_f}$				$\frac{1}{L_f}$			
8	i_{1d}^{-}				$\frac{-1}{L_f}$				$\frac{1}{L_f}$		
9										$(\frac{2}{3})P_0{}^*(\frac{-1}{v_{pd,f}^{+}{}^2})$	
10										$(\frac{-2}{3})Q_0{}^*(\frac{-1}{v_{pd,f}^{+}{}^2})$	
11											
12											

(A3)

$$A_{1c_{(11\times12)}} =$$

	1	2	3	4	5	6	7	8	9	10	11	12
1												
2	$\frac{-1}{C_f}$				$\frac{1}{C_f}$							
3		$\frac{-1}{C_f}$				$\frac{1}{C_f}$						
4			$\frac{-1}{C_f}$				$\frac{1}{C_f}$					
5				$\frac{-1}{C_f}$				$\frac{1}{C_f}$				
6												
7												
8												
9												
10												
11												

(A4)

$$A_{1d_{(11\times11)}} =$$

	1	2	3	4	5	6	7	8	9	10	11
1											$K_{i,\mathrm{PLL}}$
2											
3											
4											
5											
6	$\frac{1}{\tau_{ff}}$				$\frac{-1}{\tau_{ff}}$						
7		$\frac{1}{\tau_{ff}}$				$\frac{-1}{\tau_{ff}}$					
8			$\frac{1}{\tau_{ff}}$				$\frac{-1}{\tau_{ff}}$				
9				$\frac{1}{\tau_{ff}}$				$\frac{-1}{\tau_{ff}}$			
10	$\frac{1}{\tau_1}$								$\frac{-1}{\tau_1}$		
11		$\frac{1}{\tau_2}$								$\frac{-1}{\tau_2}$	

(A5)

For $A_{2_{(23\times23)}}$ and $B_{1_{(23\times6)}}$ matrices, the non-zero elements are as follows:

$$A_2(5,9) = \frac{K_p}{L_f}, A_2(6,10) = \frac{K_p}{L_f}, A_2(7,11) = \frac{K_p}{L_f},$$
$$A_2(8,12) = \frac{K_p}{L_f}, A_2(13,23) = K_{p,\mathrm{PLL}} \tag{A6}$$

$$B_1(1,1) = \frac{-1}{(L_1+L_0)}, B_1(2,2) = \frac{-1}{(L_1+L_0)},$$
$$B_1(3,3) = \frac{-1}{(L_1+L_0)},$$
$$B_1(4,4) = \frac{-1}{(L_1+L_0)}, B_1(9,5) = \left(\frac{2}{3}\right)\left(\frac{1}{v_{pd,f,ss}^{+}}\right),$$
$$B_1(10,6) = \left(\frac{-2}{3}\right)\left(\frac{1}{v_{pd,f,ss}^{+}}\right). \tag{A7}$$

By using the above matrices, the final state and input matrices can be obtained based on (7), in which $A = (I - A_2)^{-1}A_1$ and $B = (I - A_2)^{-1}B_1$. By defining any desired output in the system, the *C* and *D* matrices will also be obtained, and the final transfer function of the system will be expressed as

$$H(s) = C(sI - A)^{-1}B + D. \tag{A8}$$

REFERENCES

[1] Global wind energy outlook, 2018. [Online]. Available: www.gwec.net

[2] 20%Wind energy by 2030, increasing wind energy's contribution to U.S. electricity supply, U.S. Dept. Energy, Washington, DC, USA, Jul. 2008.

[3] Wind by numbers: Economic benefits of wind energy, Canadian Wind Energy Assoc., Ottawa, ON, Canada, 2018. [Online]. Available: http://www.canwea.ca

[4] M. Firouzi and G. B. Gharehpetian, "LVRT performance enhancement of DFIG-based wind farms by capacitive bridge-type fault current limiter (CBFCL)," *IEEE Trans. Sustain. Energy*, vol. 9, no. 3, pp. 1118–1125, Jul. 2018.

[5] K. Oguma and H. Akagi, "Low-voltage-ride-through (LVRT) control of an HVDC transmission system using two modular multilevel DSCC converters," *IEEE Trans. Power Electron.*, vol. 32, no. 8, pp. 5931–5942, Aug. 2017.

[6] M. M. Shabestary and Y. A. R. I. Mohamed, "Advanced voltage support and active power flow control in grid-connected converters under unbalanced conditions," *IEEE Trans. Power Electron.*, vol. 33, no. 2, pp. 1855–1864, Feb. 2018.

[7] M. Tsili and S. Papathanassiou, "A review of grid code technical requirements for wind farms," *IET Renew. Power Gener.*, vol. 3, no. 3, pp. 308–332, Sep. 2009.
[8] *Grid Code: High and Extra High Voltage*, E. ON Netz GmbH, Bayreuth, Germany, Apr. 2006. [Online]. Available: http://www.eon-netz.com
[9] *Technical Requirements for the Connection and Operation of Customer Installations to the High Voltage Network (TAB High Voltage)*, VDE-AR-N 4120, Jan. 2015.
[10] *Network Code for Requirements for Grid Connection Applicable to All Generators*, Eur. Netw. Transmiss. Syst. Oper. Elect., Brussels, Belgium, Jun. 2012.
[11] Ö. Göksu, R. Teodorescu, C. L. Bak, F. Iov, and P. C. Kjær, "Instability of wind turbine converters during current injection to low voltage grid faults and PLL frequency based stability solution," *IEEE Trans. Power Syst.*, vol. 29, no. 4, pp. 1683–1691, Jul. 2014.
[12] M. M. Shabestary, "A comparative analytical study on low-voltage ride-through reference-current-generation (LVRT-RCG) strategies in converter-interfaced DER units," M.S. thesis, Dept. Electron. Commun. Eng., Univ. Alberta, Edmonton, AB, Canada, 2014.
[13] M. M. Shabestary and Y. A. R. I. Mohamed, "An analytical method to obtain maximum allowable grid support by using grid-connected converters," *IEEE Trans. Sustain. Energy*, vol. 7, no. 4, pp. 1558–1571, Oct. 2016.
[14] R. Teodorescu *et al.*, *Grid Converters for Photovoltaic and Wind Power Systems*. New York, NY, USA: Wiley, 2011.
[15] M. M. Shabestary and Y. A. R. I. Mohamed, "Analytical expressions for multiobjective optimization of converter-based DG operation under unbalanced grid conditions," *IEEE Trans. Power Electron.*, vol. 32, no. 9, pp. 7284–7296, Sep. 2017.
[16] N. Espinoza, M. Bongiorno, and O. Carlson, "Novel LVRT testing method for wind turbines using flexible VSC technology," *IEEE Trans. Sustain. Energy*, vol. 6, no. 3, pp. 1140–1149, Jul. 2015.
[17] K. Ma, W. Chen, M. Liserre, and F. Blaabjerg, "Power controllability of three-phase converter with unbalanced AC source," *IEEE Trans. Power Electron.*, vol. 30, no. 3, pp. 1591–1604, Mar. 2015.
[18] X. Guo, X. Zhang, B. Wang, W. Wu, and J. M. Guerrero, "Asymmetrical grid fault ride-through strategy of three-phase grid-connected inverter considering network impedance impact in low-voltage grid," *IEEE Trans. Power Electron.*, vol. 29, no. 3, pp. 1064–1068, Mar. 2014.
[19] M. M. Shabestary and Y. A. R. I. Mohamed, "Analytical expressions for multiobjective optimization of converter-based DG operation under unbalanced grid conditions," *IEEE Trans. Power Electron.*, vol. 32, no. 9, pp. 7284–7296, Sep. 2017.
[20] S. Mortazavian, M. M. Shabestary, and Y. A. R. I. Mohamed, "Analysis and dynamic performance improvement of grid-connected voltage-source converters under unbalanced network conditions," *IEEE Trans. Power Electron.*, vol. 32, no. 10, pp. 8134–8149, Oct. 2017.
[21] K. Sharifabadi, L. Harnefors, H.-P. Nee, S. Norrga, and R. Teodorescu, *Design, Control, and Application of Modular Multilevel Converters for HVDC Transmission Systems*, 1st ed. New York, NY, USA: Wiley, 2016.
[22] H. C. Chen, C. T. Lee, P. T. Cheng, R. Teodorescu, and F. Blaabjerg, "A low-voltage ride-through technique for grid-connected converters with reduced power transistors stress," *IEEE Trans. Power Electron.*, vol. 31, no. 12, pp. 8562–8571, Dec. 2016.
[23] T. Neumann, T. Wijnhoven, G. Deconinck, and I. Erlich, "Enhanced dynamic voltage control of type 4 wind turbines during unbalanced grid faults," *IEEE Trans. Energy Convers.*, vol. 30, no. 4, pp. 1650–1659, Dec. 2015.
[24] M. F. M. Arani and Y. A. R. I. Mohamed, "Assessment and enhancement of a full-scale PMSG-based wind power generator performance under faults," *IEEE Trans. Energy Convers.*, vol. 31, no. 2, pp. 728–739, Jun. 2016.
[25] A. Yazdani and R. Iravani, *Voltage-Sourced Converters in Power Systems: Modeling, Control, Applications*. Hoboken, NJ, USA: Wiley, 2010.
[26] P. Kundur, *Power System Stability and Control*. New York, NY, USA: McGraw-Hill Education, 1994.
[27] A. Golieva, "Low short circuit ratio connection of wind power plants," M.Sc. thesis, Dept. Elect. Power Eng., Norwegian Univ. Sci. Technol., Trondheim, Norway, Aug. 2015.
[28] D. Zhou and F. Blaabjerg, "Optimized demagnetizing control of DFIG power converter for reduced thermal stress during symmetrical grid fault," *IEEE Trans. Power Electron.*, vol. 23, no. 12, pp. 10326–10340, Dec. 2018, doi: 10.1109/TPEL.2018.2803125.
[29] Y. Li, Q. Xu, T. Lin, J. Hu, Z. He, and R. Mai, "Analysis and design of load-independent output current or output voltage of a three-coil wireless power transfer system," *IEEE Trans. Transp. Electrific.*, vol. 4, no. 2, pp. 364–375, Jun. 2018.
[30] B. Liu, X. Shi, Y. Li, F. F. Wang, and L. M. Tolbert, "A line impedance conditioner for saturation mitigation of zigzag transformer in hybrid AC/DC transmission system considering line unbalances," *IEEE Trans. Power Electron.*, vol. 32, no. 7, pp. 5070–5086, Jul. 2017.

Shahed Mortazavian (S'15) received the M.Sc. degree in electrical and computer engineering from the Amirkabir University of Technology, Tehran, Iran, in 2013, and the Ph.D. degree in energy systems from the University of Alberta, Edmonton, AB, Canada, in 2018.

She is currently a Postdoctoral Fellow with the University of Alberta. Her research interests include dynamic analysis and control of power converters, power system analysis and stabilization, renewable energy resources, distributed generation, smart grids, fault diagnosis, and condition monitoring in power systems.

Yasser Abdel-Rady I. Mohamed (M'06–SM'11) was born in Cairo, Egypt, on November 25, 1977. He received the B.Sc. (Hons.) and M.Sc. degrees in electrical engineering from Ain Shams University, Cairo, in 2000 and 2004, respectively, and the Ph.D. degree in electrical engineering from the University of Waterloo, Waterloo, ON, Canada, in 2008.

He is currently a Professor with the Department of Electrical and Computer Engineering, University of Alberta, Edmonton, AB, Canada. His research interests include dynamics and controls of power converters, grid integration of distributed generation and renewable resources, microgrids, modeling, analysis, and control of smart grids, and electric machines and motor drives.

Dr. Mohamed is an Associate Editor for the IEEE TRANSACTIONS ON INDUSTRIAL ELECTRONICS and IEEE TRANSACTIONS ON POWER ELECTRONICS and an Editor for the IEEE TRANSACTIONS ON POWER SYSTEMS and IEEE TRANSACTIONS ON SMART GRID. He is a Registered Professional Engineer in the Province of Alberta.